https://doi.org/10.5194/egusphere-2025-523
Preprint. Discussion started: 13 February 2025
© Author(s) 2025. CC BY 4.0 License.

A fresh look at the pre-industrial air-sea carbon flux using the alkalinity budget

Alban Planchat[1,2,3], Laurent Bopp[1], and Lester Kwiatkowski[4]

[1]LMD-IPSL, CNRS, Ecole Normale Supérieure/PSL Res. Univ, Ecole Polytechnique, Sorbonne Université, Paris, 75005, France
[2]Climate and Environmental Physics, Physics Institute, University of Bern, Bern, Switzerland
[3]Oeschger Centre for Climate Change Research, University of Bern, Bern, Switzerland
[4]LOCEAN, Sorbonne Université-CNRS-IRD-MNHN, Paris, 75005, France

Correspondence: Alban Planchat (alban.planchat@unibe.ch)

Abstract. The disparities in estimates of the ocean carbon sink, whether derived from observations or models, raise questions about our ability to accurately assess its magnitude and trend over recent decades. A potential factor contributing to this inconsistency is the pre-industrial air-sea carbon flux, which is thought to arise globally from an imbalance between riverine discharge and sediment burial of carbon. The characterization of this flux is essential for isolating the anthropogenic component of the total air-sea carbon flux estimated from observations; however, it remains highly uncertain, limiting confidence in the impactful applications of the Global Carbon Budget (GCB). In this study, we propose a fresh look at the pre-industrial air-sea carbon flux using the alkalinity budget. We demonstrate the relevance of a novel theoretical framework that directly enables the calculation of the riverine/burial-driven pre-industrial carbon outgassing using both carbon and alkalinity budgets. We also introduce a practical framework to evaluate the spatial distribution of this flux through a series of ocean biogeochemical simulations. Our reassessment, grounded in existing carbon and alkalinity budgets, yields an estimated riverine/burial-driven pre-industrial carbon outgassing of 0.49 $[0.34; 0.70]$ PgC yr^{-1}, which is lower than the most recent central estimate of 0.65 ± 0.30 PgC yr^{-1}. This adjustment partially reduces the disparities between observation-based and model-derived estimates of the anthropogenic ocean carbon sink. Using a composite simulation derived from a linear combination of our sensitivity experiments, we reassess the spatial distribution of this flux, attributing 29 % to the southern region (south of 20°S), 40 % to the inter-tropical region (20°S-20°N), and 31 % to the northern region (north of 20°N). Notably, these findings represent an intermediate distribution compared to those used in the GCB over time, with recent values at 14 %, 64 %, and 22 %, and historical values at 49 %, 25 %, and 26 %. Addressing the current inconsistencies between the combined carbon and alkalinity budgets is thus an urgent priority for building confidence in the global riverine/burial-driven pre-industrial carbon outgassing, and intermodel comparisons are required to constrain its regional distribution.

1 Introduction

Accurately estimating the anthropogenic carbon sink in the ocean is crucial for gaining a deeper understanding of the underlying mechanisms, and is a prerequisite for projecting its future evolution and the climate response to future emissions scenarios

https://doi.org/10.5194/egusphere-2025-523
Preprint. Discussion started: 13 February 2025
© Author(s) 2025. CC BY 4.0 License.

(Canadell et al., 2021). This anthropogenic carbon flux is currently assessed with yearly updates by the Global Carbon Budget (GCB; Friedlingstein et al., 2024), using both observational products and model simulations employing Global Ocean Biogeochemical Models (GOBMs). Nevertheless, reconstructions based on surface ocean pCO_2 data, which constitute the primary observation-based methods, mostly exceed the model estimates, both at the global and regional scale (e.g. Hauck et al., 2020; Crisp et al., 2022; Friedlingstein et al., 2024). This disparity has grown since the early 2000s, reaching a 10 to 20 % difference over the past decade (Friedlingstein et al., 2024).

The net air-sea carbon flux derived from pCO_2-based data encompasses both anthropogenic and natural components. The natural component originates, at the global scale, from the balance between riverine discharge and the burial of organic matter (OM) and calcium carbonate ($CaCO_3$). As these external fluxes together represent a net source of carbon for the ocean, they result in a net carbon outgassing at equilibrium during the pre-industrial era. Consequently, assessing the anthropogenic carbon flux through observations requires determining the pre-industrial riverine/burial-driven air-sea carbon flux and its spatial distribution (e.g. Hauck et al., 2020; Friedlingstein et al., 2024).

Assessing this outgassing carbon flux remains highly uncertain, with estimates ranging from 0.23 to 0.78 PgC yr^{-1} (Aumont et al., 2001; Jacobson et al., 2007; Resplandy et al., 2018; Lacroix et al., 2020; Regnier et al., 2022), depending on the modeling approach used to derive them (forward or inverse) and literature estimates of riverine and burial fluxes (see Table B2). Specifically, the most recent estimate of 0.65 ± 0.30 Pg Cyr^{-1} is that used in the latest GCB release (Regnier et al., 2022; Friedlingstein et al., 2024, Table 1).

The spatial distribution of this riverine/burial-driven air-sea carbon flux is also highly uncertain and depends on the assumptions and methods used for its assessment (see Table B2). The historical value, obtained from a modeling analysis (Aumont et al., 2001), and used for a long time in the GCB, distributes this flux as follows: 49 % in the southern region, 25 % in the inter-tropical region, and 26 % in the northern region. In contrast, the latest estimate, currently used in the GCB and also based on a modeling study (Lacroix et al., 2020, Table 1), evaluates this distribution as 14 %, 64 % and 22 %, respectively, which completely reshapes the distribution of this flux.

The uncertainties associated with estimating the riverine/burial-driven pre-industrial outgassing may contribute to disparities between observation-based and model-derived estimates of the anthropogenic carbon sink, both globally and regionally (Friedlingstein et al., 2024, their Fig. 11 and 14). These disparities have emerged and disappeared without apparent reason, often in conjunction with reassessments of the riverine/burial-driven pre-industrial outgassing and its distribution, as well as the choices made within the GCB (Fig. 1 and Table 1). For instance, there was a notable global decrease in riverine/burial-driven pre-industrial outgassing from 2019 to 2020, which contributed to a significant reduction in discrepancies. Additionally, a regional shift occurred from 2022 to 2023, characterized by a reduction in bias in the southern region and a corresponding increase in the inter-tropical region.

Enhancing our understanding of the riverine/burial-driven air-sea carbon flux is critical to achieving more precise estimates of the anthropogenic carbon flux and its distribution from data-driven assessments. Numerical models are a promising approach to addressing this challenge, especially when estimating its distribution. However, at present, the representation of the pre-industrial air-sea carbon flux remains uncertain in inter-model comparison exercises like CMIP6 (the 6th phase of the Coupled

https://doi.org/10.5194/egusphere-2025-523
Preprint. Discussion started: 13 February 2025
© Author(s) 2025. CC BY 4.0 License.

Table 1. Review of the air-sea carbon outgassing from riverine/burial fluxes of carbon and Alk used in the GCBs. Both the global values and their regional distribution are presented, along with the associated references.

Air-sea carbon outgassing from riverine/burial fluxes of carbon and Alk						
GCB	Global		Distribution			
	Reference(s)	GtC yr-1	Reference	GtC yr-1 (%)		
				South	Inter-tropics	North
2023 to 2024	Regnier et al. (2022)	0.65 ± 0.3	Lacroix et al. (2020)	0.09 (14)	0.42 (64)	0.14 (22)
2022	Regnier et al. (2022)	0.65	Aumont et al. (2001)	0.32 (49)	0.16 (25)	0.17 (26)
2020 to 2021	Jacobson et al. (2007) & Resplandy et al. (2018)	0.61	Aumont et al. (2001)	0.30 (49)	0.15 (25)	0.16 (26)
2018 to 2019	Resplandy et al. (2018)	0.78	Aumont et al. (2001)	0.38 (49)	0.19 (25)	0.20 (26)
2013 to 2017	Jacobson et al. (2007)	0.45	*Not applicable*			
1959-2011	*Not applicable*					

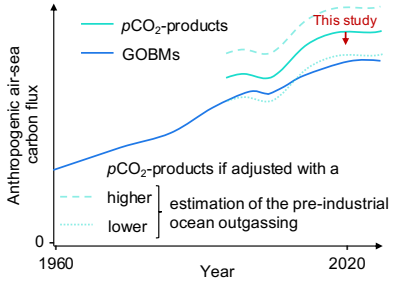

Figure 1. Schematic illustration of how a bias in evaluating the pre-industrial ocean carbon outgassing affects the assessment of the anthropogenic carbon flux based on pCO_2-products. A downward revision of the pre-industrial outgassing would decrease anthropogenic carbon flux estimates based on pCO_2-products, while an upward revision would increase it. This effect applies both globally and regionally.

Model Intercomparison Project, Eyring et al., 2016) and the 2022 GCB (Friedlingstein et al., 2024). The magnitude of this global net flux ranges from -0.73 to 0.38 PgC yr^{-1}, while its inter-hemispheric gradient, defined as the difference between its values in the northern and southern hemispheres, ranges from -0.09 to 0.82 PgC yr^{-1} (Fig. 1a).

The methods employed thus far to estimate the riverine/burial-driven air-sea carbon flux at the global scale mostly rely on closing the ocean carbon budget. However, they often exhibit limitations in addressing the ocean alkalinity budget. Alkalinity (Alk), defined as the excess of proton acceptors over proton donors, or of positive conservative charges over negative ones, plays a pivotal role in driving air-sea carbon exchanges, which are strongly dependent on the relative balance between Alk and dissolved inorganic carbon (DIC; e.g. Humphreys et al., 2018). Similar to carbon, the Alk budget is controlled by both sources and sinks at the boundaries of the oceanic domain (Middelburg et al., 2020). Conventionally, it is hypothesized that the global Alk inventory has been in equilibrium during the pre-industrial era, with Alk riverine discharge compensated by the burial of $CaCO_3$ (e.g. Revelle and Suess, 1957; Aumont et al., 2001; Planchat et al., 2023). Nonetheless, the hypothesis of a potentially disequilibrated global Alk inventory during the pre-industrial era remains plausible, considering the overall balance

https://doi.org/10.5194/egusphere-2025-523
Preprint. Discussion started: 13 February 2025
© Author(s) 2025. CC BY 4.0 License.

of Alk sources and sinks (e.g. Milliman, 1993; Middelburg et al., 2020). Such an Alk inventory disequilibrium would drive a disequilibrium in the global carbon inventory and affect the air-sea carbon flux. This hypothesis gains additional support from paleoclimatology studies, which suggest the possibility of an Alk inventory disequilibrium due to additional $CaCO_3$ burial (e.g. Cartapanis et al., 2018) or a carbonate compensation mechanism involving biological processes alongside riverine input (Boudreau et al., 2018).

Here, we reevaluate the riverine/burial-driven pre-industrial air-sea carbon flux by introducing a theoretical framework that uses both carbon and Alk budgets. After testing the approach through a series of sensitivity simulations using a global biogeochemical model and covering a broad spectrum of uncertainties related to riverine and burial fluxes, we derive a new estimate of the riverine/burial-driven pre-industrial air-sea carbon flux based on existing carbon and Alk budgets. Subsequently, using a practical framework, we reassess the spatial distribution of the flux by constructing a composite simulated estimate from a linear combination of our sensitivity simulations.

2 Methods

2.1 Overview and definitions

2.1.1 Global air-sea carbon flux

The collection of surface ocean pCO_2 data, and associated statistical methods, only allow for the direct reconstruction of the contemporary air-sea carbon flux ($F_{\text{cont.}}^{\text{C, air}-\text{sea}}$), which encompasses both an anthropogenic ($F_{\text{ant.}}^{\text{C, air}-\text{sea}}$) and a natural ($F_{\text{nat.}}^{\text{C, air}-\text{sea}}$) component (e.g. Hauck et al., 2020), as follows:

$$F_{\text{cont.}}^{\text{C, air}-\text{sea}} = F_{\text{ant.}}^{\text{C, air}-\text{sea}} + F_{\text{nat.}}^{\text{C, air}-\text{sea}} \tag{1}$$

where all fluxes are directed into the ocean (consistent throughout this manuscript). Therefore, it is crucial to determine the natural component to extract the anthropogenic carbon flux from pCO_2-based products. Within the anthropogenic carbon flux, we incorporate the perturbation of the natural carbon flux in response to climate change, ensuring that $F_{\text{ant.}}^{\text{C, air}-\text{sea}}$ genuinely represents the carbon sink resulting from all human-induced disturbances (e.g. Hauck et al., 2020). Additionally, we assume that there have been no alterations to riverine and burial fluxes in response to the Anthropocene, allowing us to directly consider $F_{\text{nat.}}^{\text{C, air}-\text{sea}}$ as the riverine/burial-driven pre-industrial (mention generally omitted hereafter) air-sea carbon flux ($F_{\text{riv./bur.}}^{\text{C, air}-\text{sea}}$), i.e.:

$$F_{\text{nat.}}^{\text{C, air}-\text{sea}} = F_{\text{riv./bur.}}^{\text{C, air}-\text{sea}} \tag{2}$$

The anthropogenic carbon flux can then be derived from pCO_2-based data as follows:

$$F_{\text{ant.}}^{\text{C, air}-\text{sea}} = F_{\text{cont.}}^{\text{C, air}-\text{sea}} - F_{\text{riv./bur.}}^{\text{C, air}-\text{sea}} \tag{3}$$

https://doi.org/10.5194/egusphere-2025-523
Preprint. Discussion started: 13 February 2025
© Author(s) 2025. CC BY 4.0 License.

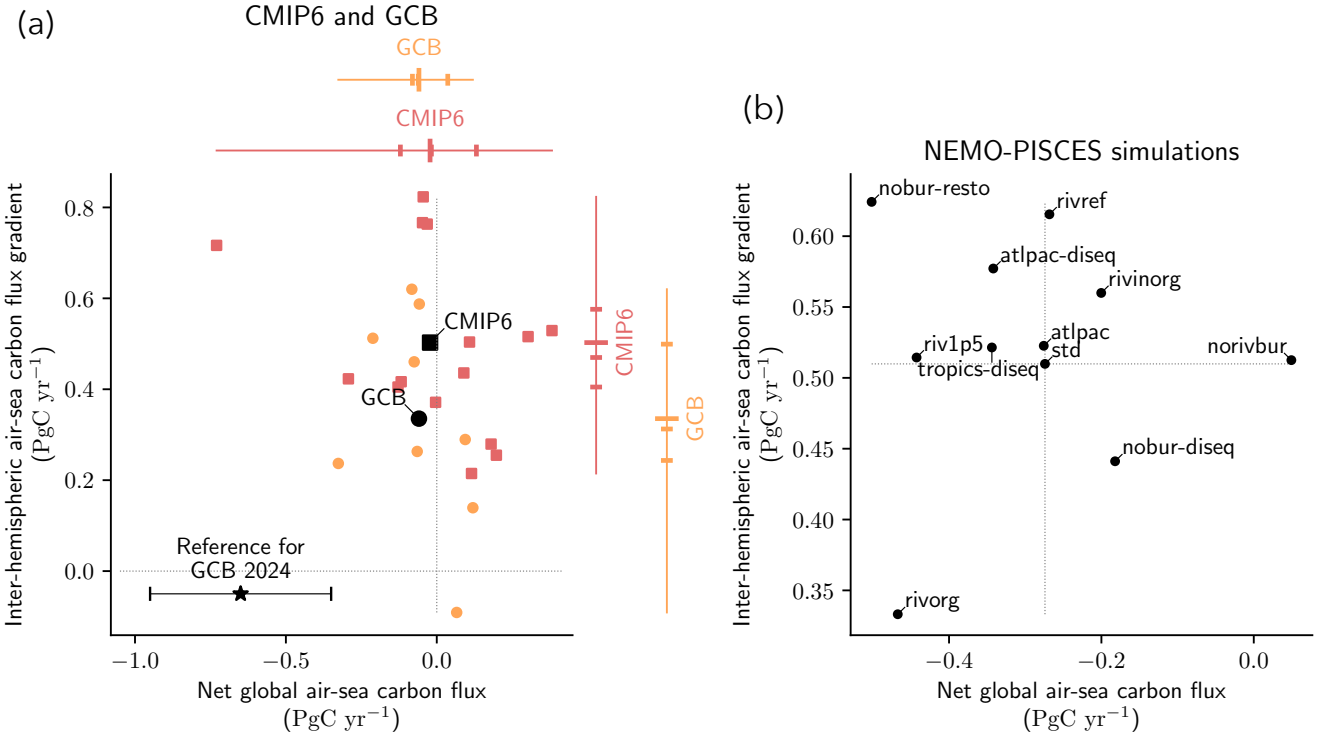

Figure 2. Pre-industrial air-sea carbon flux from models. The globally integrated pre-industrial flux (x-axis) and its interhemispheric gradient (y-axis) are indicated for (a) CMIP6 ESMs and GCB GOBMs, as well as for (b) the NEMO-PISCES sensitivity simulations. (a) The 15 CMIP6 ESMs (10 GCB GOBMs; see Appendix A1) are plotted with red squares (orange circles). The black square and circle refer to the CMIP6 and GCB ensemble means. The CMIP6 and GCB ensemble ranges (line), mean (major tick) and quartiles (minor ticks) are respectively displayed to the top and right in red and orange. The star refers to the reference value used in the GCB 2024 (Table 1; Friedlingstein et al., 2024). The inter-hemispheric air-sea carbon flux gradient is defined as the difference between its values in the northern and southern hemispheres (Sect. 2.1.3).

When assuming a global Alk inventory equilibrium, the global riverine/burial-driven air-sea carbon flux can be directly deduced from the carbon budget at equilibrium (e.g. Regnier et al., 2022):

$$F^{\mathrm{C,\ air-sea}}_{\mathrm{riv./bur.}} + F^{\mathrm{C,\ riv./bur.}} = 0 \tag{4}$$

with:

$$F^{\mathrm{C,\ riv./bur.}} = F^{\mathrm{C,\ riv.}} + F^{\mathrm{C,\ bur.\ org.}} + F^{\mathrm{C,\ bur.\ inorg.}} + F^{\mathrm{C,\ minor\ components}} \tag{5}$$

where 'riv.' stands for 'riverine discharge', 'bur. org.' for 'OM burial', 'bur. inorg.' for '$CaCO_3$ burial', and 'minor components' encompass other minor external fluxes, such as carbon release by mid-ocean ridges and groundwater discharge. Thus, assuming a global Alk inventory equilibrium, the riverine/burial-driven air-sea carbon flux is the opposite of the riverine and burial fluxes

https://doi.org/10.5194/egusphere-2025-523
Preprint. Discussion started: 13 February 2025
© Author(s) 2025. CC BY 4.0 License.

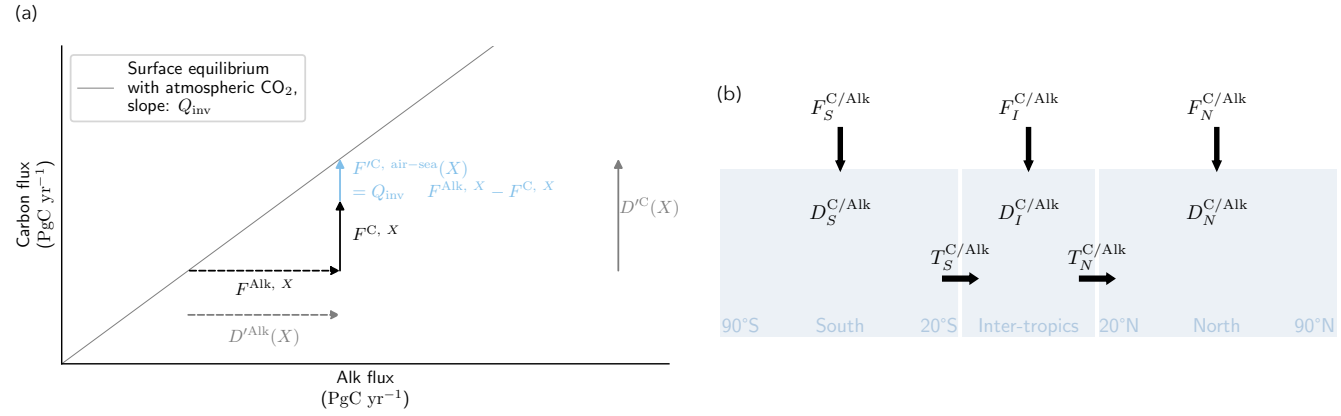

Figure 3. Schematics of the theroetical framework introduced in this manuscript. (a) Schematic construction for a process X (e.g. $CaCO_3$ burial), impacting carbon ($F^{C,\ X}$) and Alk ($F^{Alk,\ X}$), of the air-sea carbon flux resulting from the associated local imbalance ($F'^{C,\ air-sea}(X)$), as well as the related disequilibrium in carbon and Alk ($D'^{C/Alk}(X)$). The surface equilibrium with atmospheric CO_2 is represented by a solid grey line. Carbon (Alk) fluxes are represented through solid (dashed) arrows, and the colors of the arrows is consistent with what is used throughout the manuscript (e.g. Fig. 2). The combination of the Alk and carbon fluxes associated with the process X results in a disequilibrium with the atmospheric CO_2 concentration, and requires an air-sea carbon flux to restore equilibrium. (b) Schematic diagram of carbon and Alk budgets by ocean region. $F^{C/Alk}$ and $T^{C/Alk}$ respectively refer to the total external fluxes (directed into the ocean) and to the northward transport of carbon and Alk. $D^{C/Alk}$ corresponds to the carbon and Alk inventory disequilibria in each basin. S, I and N refer to the different ocean regions, respectively the southern hemisphere, the inter-tropical zone, and the northern hemisphere.

of carbon:

$$F^{C,\ air-sea}_{riv./bur.} = -F^{C,\ riv./bur.} \tag{6}$$

However, when considering a global Alk inventory not in equilibrium, it becomes essential to account for the Alk balance in order to infer the riverine/burial-driven air-sea carbon flux:

$$F^{Alk,\ riv./bur.} = F^{Alk,\ riv.} + F^{Alk,\ bur.\ org.} + F^{Alk,\ bur.\ inorg.} + F^{Alk,\ minor\ components} \tag{7}$$

where 'minor components' encompass this time other minor external fluxes such as anaerobic processes, silicate weathering, and groundwater discharge. Importantly, any imbalance in alkalinity (Alk) triggers a corresponding carbon flux to achieve equilibrium with the atmosphere. To estimate this flux, we extend the conceptual framework introduced by Humphreys et al. (2018) by utilizing a phase diagram (Alk, DIC) in the form of an Alk and DIC flux diagram, while operating on a global scale (Fig. 3a). For any flux affecting carbon and/or Alk, it is possible to derive an air-sea carbon flux and the associated global carbon and Alk inventory imbalances. This approach relies on the equilibrium relationship between the Alk-DIC pair and the atmospheric CO_2 concentration. At global scale, at equilibrium, any deviation in Alk is directly proportional to a DIC anomaly,

https://doi.org/10.5194/egusphere-2025-523
Preprint. Discussion started: 13 February 2025
© Author(s) 2025. CC BY 4.0 License.

and this proportionality coefficient can be estimated with high precision, as follows:

$$Q_{\mathrm{inv}} \simeq \frac{\mathrm{Alk}}{3 \cdot \mathrm{Alk} - 2 \cdot \mathrm{DIC}} \tag{8}$$

where Q_{inv}, as previously defined in Planchat et al. (2023), represents the inverse of the 'isocapnic quotient' approximation introduced by Humphreys et al. (2018). In the case of an ocean at equilibrium (see Fig. B1), every external flux X (e.g. riverine discharge) that exerts an impact on carbon ($F^{\mathrm{C},\ X}$) and/or Alk ($F^{\mathrm{Alk},\ X}$), results in a global imbalance, shifting the surface ocean away from equilibrium with the atmosphere. Specifically, this requires an air-sea carbon flux ($F^{\mathrm{C,air-sea}}(X)$; Fig. 3a) to maintain global equilibrium with respect to the atmospheric CO_2 concentration. This also leads to disequilibria in global carbon and Alk inventories (D^{C} and D^{Alk}, respectively). In summary, for any given process X, we can define:

$$\begin{cases} F^{\mathrm{C},\ \mathrm{air-sea}}(X) = F^{\mathrm{Alk},\ X} \cdot Q_{\mathrm{inv}} - F^{\mathrm{C},\ X} \\ D^{\mathrm{C}}(X) = F^{\mathrm{Alk},\ X} \cdot Q_{\mathrm{inv}} \\ D^{\mathrm{Alk}}(X) = F^{\mathrm{Alk},\ X} \end{cases} \tag{9}$$

Applying this theoretical framework to the total external carbon and Alk fluxes ($F^{\mathrm{C},\ \mathrm{riv./bur.}}$ and $F^{\mathrm{Alk},\ \mathrm{riv./bur.}}$, respectively), we can deduce the riverine/burial-driven air-sea carbon flux ($F^{\mathrm{C},\ \mathrm{air-sea}}_{\mathrm{riv./bur.}}$) and the respective disequilibria in global carbon and Alk inventories as follows:

$$\begin{cases} F^{\mathrm{C},\ \mathrm{air-sea}}_{\mathrm{riv./bur.}} = F^{\mathrm{Alk},\ \mathrm{riv./bur.}} \cdot Q_{\mathrm{inv}} - F^{\mathrm{C},\ \mathrm{riv./bur.}} \\ D^{\mathrm{C}} = F^{\mathrm{Alk},\ \mathrm{riv./bur.}} \cdot Q_{\mathrm{inv}} \\ D^{\mathrm{Alk}} = F^{\mathrm{Alk},\ \mathrm{riv./bur.}} \end{cases} \tag{10}$$

It is worth noting that this general expression also applies to the specific case where the global Alk inventory is in equilibrium ($F^{\mathrm{Alk},\ \mathrm{riv./bur.}} = 0$).

2.1.2 Air-sea carbon flux from local/regional imbalance

While it is feasible to establish a direct relationship between the influence of carbon and Alk fluxes on the net air-sea carbon flux at the global scale under the assumption of an equilibrated ocean, this approach is not directly applicable at the local or regional scale due to the complex dynamics of ocean circulation, which transport both carbon and Alk. To gain a deeper understanding of the factors shaping the spatial distribution of the riverine/burial-driven air-sea carbon flux, we expand upon the theoretical framework previously outlined for the global scale (refer to Section 2.1.1) and adapt it for application at local and regional scales.

Indeed, at local/regional scale, this conceptual tool only permits estimates of a potential air-sea carbon flux resulting from a local/regional carbon:Alk imbalance (Fig. 3a). Specifically, this air-sea carbon flux, defined locally/regionally, only becomes effective at equilibrium and at the global scale. There is indeed no guarantee of its local/regional applicability due to the transport of the induced carbon:Alk local/regional imbalance. In summary, we can adapt Eq. 9 for any process X affecting carbon and/or Alk, and for a given latitude (lat) with zonally integrated values, or for a specific ocean region (south: S, inter-

https://doi.org/10.5194/egusphere-2025-523
Preprint. Discussion started: 13 February 2025
© Author(s) 2025. CC BY 4.0 License.

tropics: I, north: N):

$$\begin{cases} F'^{\mathrm{C,\ air-sea}}_{\mathrm{lat}/N/S/I}(X) = F^{\mathrm{Alk},\ X}_{\mathrm{lat}/N/S/I} \cdot Q_{\mathrm{inv,\ lat}/N/S/I} - F^{\mathrm{C},\ X}_{\mathrm{lat}/N/S/I} \\ D'^{\mathrm{C},\ X}_{\mathrm{lat}/N/S/I} = F^{\mathrm{Alk},\ X}_{\mathrm{lat}/N/S/I} \cdot Q_{\mathrm{inv,\ lat}/N/S/I} \\ D'^{\mathrm{Alk},\ X}_{\mathrm{lat}/N/S/I} = F^{\mathrm{Alk},\ X}_{\mathrm{lat}/N/S/I} \end{cases} \tag{11}$$

where $F'^{\mathrm{C,\ air-sea}}_{\mathrm{lat}/N/S/I}(X)$ is the air-sea carbon flux from local/regional imbalance, and $D'^{\mathrm{C},\ X}_{\mathrm{lat}/N/S/I}$ as well as $D'^{\mathrm{Alk},\ X}_{\mathrm{lat}/N/S/I}$ are the associated disequilibria entailed for the global carbon and Alk inventories, respectively (Fig. 3a). This comprehensive set of equations is essential to understanding the extent to which the local/regional carbon:Alk imbalance can drive the global air-sea carbon flux as well, as carbon and Alk disequilibria. In this context, these remain potential fluxes and potential disequilibria, which is why a prime is used in their notation to distinguish them from global scale fluxes (Eq. 9).

2.1.3 Defining the inter-hemispheric flux gradient

Ocean circulation and carbon pumps within the ocean induce an asymmetry in the ocean on either side of the Intertropical Convergence Zone (ITCZ), which serves as an inter-hemispheric transport barrier. This asymmetry notably slows down the atmospheric carbon flux from the northern to the southern hemispheres (Murnane et al., 1999). To assess the significance of this asymmetry on the air-sea carbon flux, particularly its components associated with riverine and burial fluxes, we provide two metrics for large-scale inter-hemispheric fluxes: (i) the inter-hemispheric air-sea carbon flux gradient (G), which is defined as the integrated net flux north of 20°N ($F_N^{\mathrm{C,\ air-sea}}$) minus that south of 20°S ($F_S^{\mathrm{C,\ air-sea}}$):

$$G = F_N^{\mathrm{C,\ air-sea}} - F_S^{\mathrm{C,\ air-sea}} \tag{12}$$

and (ii) the inter-hemispheric ocean transport of carbon (T^{C}) and Alk (T^{Alk}), both directed northward, defined as the mean transport between 20°N ($T_N^{\mathrm{C/Alk}}$) and 20°S ($T_S^{\mathrm{C/Alk}}$):

$$T^{\mathrm{C/Alk}} = \frac{1}{2} \cdot \left(T_N^{\mathrm{C/Alk}} + T_S^{\mathrm{C/Alk}} \right) \tag{13}$$

These two metrics rely on the subdivision of the ocean into two poleward basins, one south of 20°S and the other north of 20°N, separated by an intertropical basin (Fig. 3b and see Appendix A4; e.g. Aumont et al., 2001; Resplandy et al., 2018).

In this context, total carbon and Alk regional fluxes can be written as follows:

$$\begin{cases} F^{\mathrm{C}}_{N/S/I} = F^{\mathrm{C,\ air-sea}}_{N/S/I} + F^{\mathrm{C,\ riv./bur.}}_{N/S/I} \\ F^{\mathrm{Alk}}_{N/S/I} = F^{\mathrm{Alk,\ riv./bur.}}_{N/S/I} \end{cases} \tag{14}$$

Specifically, by considering these fluxes ($F^{\mathrm{C/Alk}}_{N,S,I}$) along with regional carbon and Alk disequilibria ($D^{\mathrm{C/Alk}}_{N,S,I}$) and assuming an ocean at equilibrium (see Fig. B1), we derive two expressions for the ocean transport of carbon and Alk through their respective budget closure equations ($T^{\mathrm{C/Alk}}_{N/S}$):

$$\begin{cases} T^{\mathrm{C/Alk}}_{N/S} + F^{\mathrm{C/Alk}}_{\geq 20°N/20°S} + D^{\mathrm{C/Alk}}_{\geq 20°N/20°S} = 0 \\ -T^{\mathrm{C/Alk}}_{N/S} + F^{\mathrm{C/Alk}}_{<20°N/20°S} + D^{\mathrm{C/Alk}}_{<20°N/20°S} = 0 \end{cases} \tag{15}$$

https://doi.org/10.5194/egusphere-2025-523
Preprint. Discussion started: 13 February 2025
© Author(s) 2025. CC BY 4.0 License.

Hence, we define the ocean transport of carbon and Alk as the average of its two expressions (Eq. 15; Fig. 3b):

$$T_{N/S}^{\mathrm{C/Alk}} = \frac{1}{2} \cdot \left[\left(F_{<20^\circ N/20^\circ S}^{\mathrm{C/Alk}} + D_{<20^\circ N/20^\circ S}^{\mathrm{C/Alk}} \right) - \left(F_{\geq 20^\circ N/20^\circ S}^{\mathrm{C/Alk}} + D_{\geq 20^\circ N/20^\circ S}^{\mathrm{C/Alk}} \right) \right] \tag{16}$$

In particular:

$$\begin{cases} T_N^{\mathrm{C/Alk}} = \frac{1}{2} \cdot \left[\left(F_S^{\mathrm{C/Alk}} + D_S^{\mathrm{C/Alk}} + F_I^{\mathrm{C/Alk}} + D_I^{\mathrm{C/Alk}} \right) - \left(F_N^{\mathrm{C/Alk}} + D_N^{\mathrm{C/Alk}} \right) \right] \\ T_S^{\mathrm{C/Alk}} = \frac{1}{2} \cdot \left[\left(F_S^{\mathrm{C/Alk}} + D_S^{\mathrm{C/Alk}} \right) - \left(F_I^{\mathrm{C/Alk}} + D_I^{\mathrm{C/Alk}} + F_N^{\mathrm{C/Alk}} + D_N^{\mathrm{C/Alk}} \right) \right] \end{cases} \tag{17}$$

from which an expression of the inter-hemispheric transport of carbon and Alk (Eq. 13) can be derived:

$$T^{\mathrm{C/Alk}} = \frac{1}{2} \cdot \left[\left(F_S^{\mathrm{C/Alk}} + D_S^{\mathrm{C/Alk}} \right) - \left(F_N^{\mathrm{C/Alk}} + D_N^{\mathrm{C/Alk}} \right) \right] \tag{18}$$

Subsequently, the inter-hemispheric air-sea carbon flux gradient is equivalent to:

$$G = \underbrace{-2 \cdot T^{\mathrm{C}}}_{\text{Transport component}} \underbrace{- \left(F_N^{\mathrm{C,\ riv./bur.}} - F_S^{\mathrm{C,\ riv./bur.}} \right) - \left(D_N^{\mathrm{C}} - D_S^{\mathrm{C}} \right)}_{\text{Riverine and burial component}} \tag{19}$$

At first glance, it may appear that this expression is exclusively formulated in terms of carbon, seemingly without any consideration of Alk. However, Alk plays a subtle yet integral role in this equation. Firstly, because T^C depends on both the southern and northern air-sea carbon fluxes (Eq. 18 and 14), and these regional fluxes are chemically driven by the relative imbalance between Alk and DIC. Secondly, the disequilibrium in the carbon content of the northern and southern oceans (D_N^{C} and D_S^{C}, respectively) is directly linked to the disequilibrium in Alk content (Eq. 11). Thus, the role of Alk is intricately interwoven within the formulation of G (Eq. 19).

2.2 Simulations

2.2.1 Model and configuration

As part of the NEMO (Nucleus for European Modelling of the Ocean) suite of models, we used here the marine biogeochemical model PISCES (Pelagic Interactions Scheme for Carbon and Ecosystem Studies) to refine our estimation of the pre-industrial air-sea carbon flux. This refinement involved a comprehensive consideration of both the carbon and Alk budgets, with a specific focus on external fluxes, notably $CaCO_3$ burial. While globally resembling PISCES-v2, as detailed in Aumont et al. (2015) and utilized in IPSL-CM6A-LR (Boucher et al., 2020), we introduced two key modifications in PISCES: (i) an adjustment to the N-fixation parameterization, following Bopp et al. (2022), and (ii) an adaptation of the burial fraction of $CaCO_3$ to maintain the global Alk inventory without necessitating an Alk restoring scheme (see Planchat et al., 2023, their Appendix A2 for details). Our simulations were conducted offline using a tripolar ORCA (orthogonal curvilinear ocean mesh) grid with a nominal resolution of 2° and included 30 vertical levels. The ocean physics were derived from pre-industrial simulations of IPSL-CM5A-LR (Dufresne et al., 2013, based on NEMOv3.2), with a repeated 500-yr period, and a fixed and homogeneous atmospheric CO_2 concentration of 284 ppm at the ocean surface.

https://doi.org/10.5194/egusphere-2025-523
Preprint. Discussion started: 13 February 2025
© Author(s) 2025. CC BY 4.0 License.

Table 2. Summary of the NEMO-PISCES sensitivity simulations with a short description (see Sect. A2 and Table A1 for more details).

Simulation	Description	Alk inventory
std	Standard (riverine discharge, as well as OM and $CaCO_3$ burial simulated)	Equilibrium
norivbur	No external fluxes of carbon and Alk, except air-sea carbon fluxes	Equilibrium
rivref	Refractory organic riverine discharge	Equilibrium
rivorg	Fully organic riverine discharge	Equilibrium
rivinorg	Fully inorganic riverine discharge	Equilibrium
riv1p5	Riverine discharge of carbon and Alk multiplied by 1.5	Equilibrium
nosed-resto	No OM and $CaCO_3$ burial, but restoration of the Alk content	Equilibrium
nosed-diseq	No OM and $CaCO_3$ burial	Disequilibrium
atlpac	Constrained balance of extra $CaCO_3$ burial/dissolution between the deep Atlantic/Pacific	Equilibrium
atlpac-diseq	Constrained imbalance of extra $CaCO_3$ burial/dissolution between the deep Atlantic/Pacific (-0.10 PgC yr-1)	Disequilibrium
tropics-diseq	Constrained extra $CaCO_3$ burial in the shallow tropics (-0.10 PgC yr-1)	Disequilibrium

To ensure model stability and attainment of a steady state (i.e. stable air-sea carbon flux; e.g. Orr et al., 2017, see Fig. B1), all simulations presented below used the same initial conditions and have been run 2550 yr after an initial 500-yr spin-up using the standard configuration (Sect. 2.2.2). We calculated the carbon and Alk budgets related to their associated external sources/sinks using data from the last 50 yr of the simulations. The carbon and Alk inventory disequilibria were estimated through linear regression over the same period.

2.2.2 Standard simulation (std) and its riverine/burial component

The standard simulation (referred to as 'std'), based on the standard configuration described above, involves carbon and Alk riverine supply as well as organic matter and $CaCO_3$ burial. Riverine supply of carbon and Alk is based on output from the Global Erosion Model (GEM) of Ludwig et al. (1996) and considers both inorganic and organic carbon riverine discharge (0.37 and 0.14 PgC yr^{-1}, respectively). Carbon and Alk are added at river mouths using a monthly climatology that is applied recursively. The inorganic fraction is supposed to be in the form of bicarbonate ions and thus affects both DIC and Alk in a similar manner. The organic fraction is assumed to be fully labile and remineralizes instantaneously at the river mouth, thus impacting only DIC. This simulation also includes the burial of OM and $CaCO_3$ produced by pelagic organisms, which is exported to the ocean interior and only partially remineralized or dissolved in the water column and at the seafloor. These combined fluxes constitute the riverine and burial fluxes (Eq. 5 and 7), which, as introduced in Sect. 2.1.1, lead to the riverine/burial-driven air-sea carbon flux.

While at the global scale, the net air-sea carbon flux directly corresponds to the riverine/burial-driven air-sea carbon flux (Eq. 2), at the local/regional scale, the air-sea carbon flux ($F_{\mathrm{nat.}}^{\mathrm{C,\ air-sea}}$) can be decomposed into two components: one associated with the functioning of the ocean carbon pumps ($F_{\mathrm{pump}}^{\mathrm{C,\ air-sea}}$) and the other associated with the riverine and burial fluxes ($F_{\mathrm{riv./bur.}}^{\mathrm{C,\ air-sea}}$), which is our primary focus. Thus, for a given latitude (lat) with zonally integrated values or for a specific ocean

https://doi.org/10.5194/egusphere-2025-523
Preprint. Discussion started: 13 February 2025
© Author(s) 2025. CC BY 4.0 License.

region (south: S, inter-tropics: I, north: N):

$$F^{\mathrm{C,\ air-sea}}_{\mathrm{nat.,\ lat}/N/S/I} = F^{\mathrm{C,\ air-sea}}_{\mathrm{pump,\ lat}/N/S/I} + F^{\mathrm{C,\ air-sea}}_{\mathrm{riv./bur.,\ lat}/N/S/I}. \tag{20}$$

To isolate the riverine/burial-driven component, a simulation without riverine and burial fluxes was conducted (referred to as 'norivbur') which simulates only the component of the flux associated with the ocean carbon pumps. This allows us to determine the riverine/burial-driven air-sea carbon flux, including its spatial distribution, by taking the difference between the std and norivbur simulations:

$$F^{\mathrm{C,\ air-sea}}_{\mathrm{riv./bur.,\ lat}/N/S/I} = F^{\mathrm{C,\ air-sea}}_{\mathrm{nat.,\ lat}/N/S/I}(\mathrm{std}) - F^{\mathrm{C,\ air-sea}}_{\mathrm{nat.,\ lat}/N/S/I}(\mathrm{norivbur}). \tag{21}$$

where the 'nat.' label was omitted since the simulations were conducted under pre-industrial conditions, and therefore, no anthropogenic component was included.

2.2.3 Sensitivity simulations and global estimate

The set of sensitivity simulations covers a broad range of perturbations to the carbon and Alk riverine and burial fluxes. These simulations aim to assess the effects of different assumptions regarding these external fluxes on the riverine/burial-driven air-sea carbon flux (Table 2, Fig.2b; see Appendix A2).

First, we introduced variations in the magnitude and characteristics of riverine inputs, which, by closing the Alk budget, also influenced $CaCO_3$ burial. In 'rivref', the OM riverine discharge was considered fully refractory (i.e. persisting on a time-scale longer than that of ocean circulation), in contrast to the lability assumption from the standard simulation. We explored fully organic and inorganic riverine discharges in 'rivorg' and 'rivinorg', respectively. Additionally, we increased riverine discharge by a factor of 1.5 in 'riv1p5'. Second, we disabled OM and $CaCO_3$ burial, artificially restoring Alk in 'nobur-resto', or assuming Alk disequilibrium in 'nobur-diseq'. Third, we introduced additional $CaCO_3$ burial/dissolution between the Atlantic and Pacific, maintaining an Alk equilibrium in 'atlpac', or not in 'atlpac-diseq', and additional $CaCO_3$ burial in the tropics, resulting in an Alk disequilibrium in 'tropics-diseq'. In all our sensitivity simulations, the '-diseq' suffix indicates an Alk disequilibrium, i.e. an increasing or decreasing global Alk inventory while maintaining a steady-state air-sea carbon flux. Furthermore, it is important to note that these variations only directly affected carbon and Alk, with nutrient fluxes left unaltered to avoid influencing OM and $CaCO_3$ production. Finally, we report that at the global scale, for the standard simulation, $Q_{\mathrm{inv}} \simeq 0.797$ (Eq. 8), and this coefficient exhibits minimal variation across all sensitivity simulations considered (< 0.002 in absolute terms).

The theoretical framework introduced in this study (Sect. 2.1.1) is evaluated through our set of sensitivity simulations. It is then used directly to estimate the global magnitude of the pre-industrial riverine/burial-driven air-sea carbon flux and to investigate the global carbon and Alk inventory disequilibria (Eq. 10) from the existing carbon and Alk budgets, which include all oceanic external sources/sinks of carbon and Alk. We used the most recent carbon (Regnier et al., 2022) and Alk (Middelburg et al., 2020) budgets, although they are independent of each other and partly inconsistent (Table 3). For instance, the gap in the $CaCO_3$ burial (0.24 versus 0.35 PgC yr^{-1}) would drive a 0.22 PgC yr^{-1} difference in the Alk budget. We took great care to account for the uncertainties/extremes associated with the various external sources/sinks of carbon and Alk.

https://doi.org/10.5194/egusphere-2025-523
Preprint. Discussion started: 13 February 2025
© Author(s) 2025. CC BY 4.0 License.

2.3 Composite simulated estimate and distribution

A practical framework was then developed, presented as an alternative method for estimating the distribution of the pre-industrial riverine/burial-driven air-sea carbon flux, specifically its inter-hemispheric partitioning. For each literature estimate of the various external sources/sinks of carbon and Alk, we constructed a skewed Gaussian distribution to match the median/mean value and the uncertainty/extreme range. To achieve this, we followed a two-step process. First, we created a triangular distribution based on the estimated median/mean value and the extremes (minimum and maximum) using Python's 'random.triangular' function from the *numpy* library. Then, we employed the 'stats.skewnorm.fit' function from the *scipy* library in Python to fit a skewed Gaussian probability density function (PDF) to this triangular distribution. This approach ensured that we maintained the integrity of the extreme and median/mean values obtained from the literature while working with continuous PDFs.

To derive the distribution of the pre-industrial riverine/burial-driven air-sea carbon flux, we constructed a composite simulated estimate by linearly combining our sensitivity simulations. This process aimed to align the riverine and burial fluxes of the composite simulated estimate with literature estimates (Middelburg et al., 2020; Regnier et al., 2022) and involved four steps (see Fig. A2, and Table 3). We began with the riverine/burial-driven air-sea carbon flux from the standard simulation (extracted from std minus norivbur) in the first step. In the second step, our objective was to match the riverine discharge and OM burial of carbon in the composite simulated estimate with the literature estimate, achieved by using the simulation where the riverine discharge was multiplied by 1.5 (extracted from riv1p5 minus std). The third step focused on matching the riverine discharge and OM burial of Alk, using the simulation where the riverine discharge was entirely inorganic (extracted from rivinorg minus std), ensuring no impact on the previously matched values of the riverine discharge and OM burial of carbon. Finally, in the fourth step, we aimed to match the $CaCO_3$ burial of Alk by using the simulation with an additional $CaCO_3$ burial/dissolution with an Alk disequilibrium (extracted from atlpac-diseq minus std), without affecting the previously matched values of the riverine discharge and OM burial of carbon and Alk. Given the intrinsic link between $CaCO_3$ burial effect on Alk and DIC with a 2:1 ratio, Step 4 should also enable to match the $CaCO_3$ burial of carbon. However, due to the inconsistency between the two most recent budgets for carbon and Alk (Table 3), an extra step was required, equivalent to Step 3, but only considering the $CaCO_3$ burial of carbon in excess. In summary, this composite simulated estimate, built on a linear combination of our sensitivity simulations constrained by external carbon and Alk fluxes from the literature, provides an alternative view of the distribution of the pre-industrial riverine/burial-driven air-sea carbon flux.

3 Results and discussion

3.1 Pre-industrial air-sea carbon flux and its riverine/burial-driven component

In the pre-industrial era, the simulated air-sea carbon flux, derived from the standard simulation (std), remains stable at $-0.27\ \mathrm{PgC\ yr^{-1}}$ (see Fig. B3a), indicating a net global ocean outgassing. However, the distribution of the surface air-sea carbon flux exhibits considerable heterogeneity among different regions, primarily driven by ocean circulation patterns (Fig. 4a).

https://doi.org/10.5194/egusphere-2025-523
Preprint. Discussion started: 13 February 2025
© Author(s) 2025. CC BY 4.0 License.

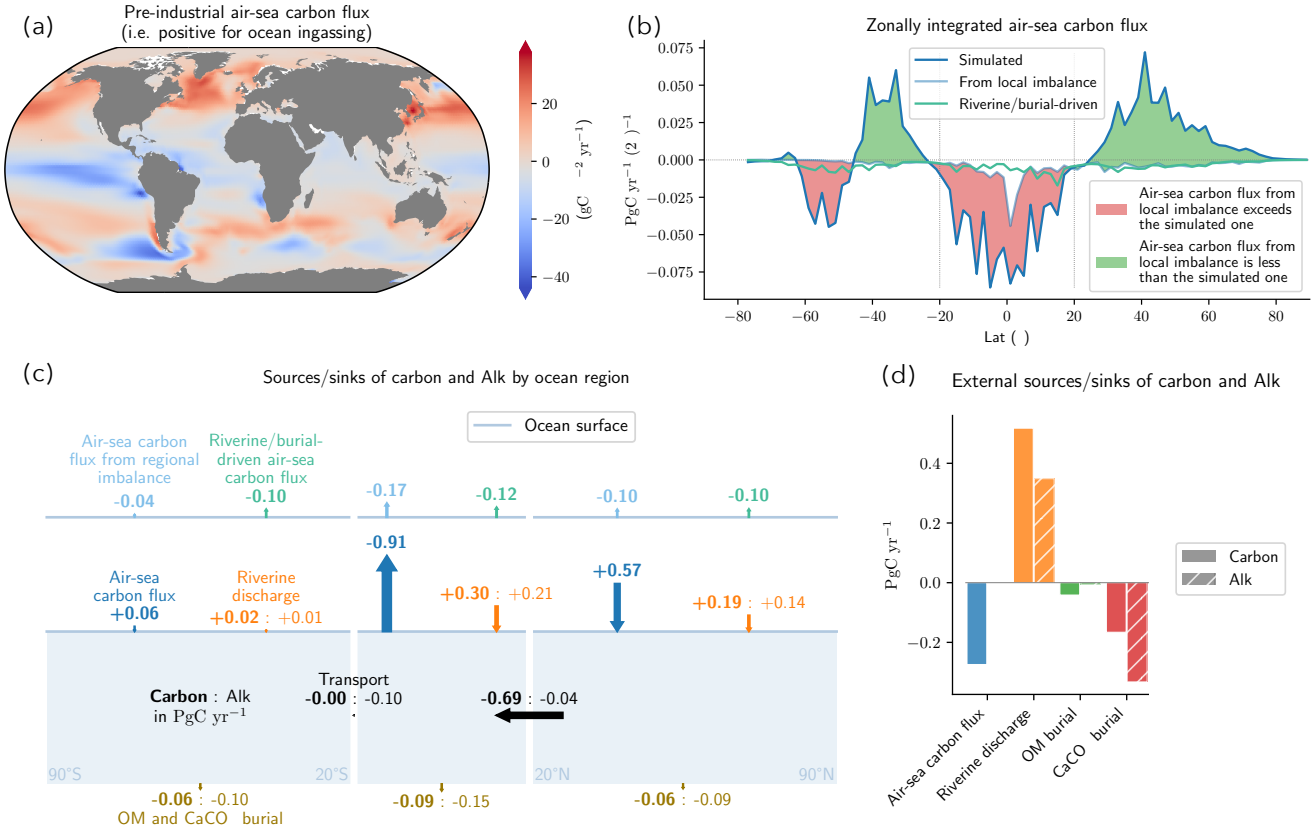

Figure 4. Description of the standard NEMO-PISCES simulation (std; see Fig. B2 for additional elements). (a) Map of the pre-industrial air-sea carbon flux, where positive values indicate ocean ingassing. (b) Zonally integrated air-sea carbon fluxes (dark blue), derived from local imbalance (light blue), and the riverine/burial-driven component (aquamarine). When the local imbalance exceeds (is less than) the simulated air-sea carbon flux, the area in between is shaded in red (green). (c) Partitioning of the riverine (orange) and burial (dark gold) fluxes by ocean region (southern, inter-tropical, and northern). The fluxes, in petagrams of carbon per year (PgC yr^{-1}) for carbon (in bold) and Alk (in normal font), are directed by arrows, with orientation indicating the sign, and size reflecting the absolute magnitude of the flux. The partitioning of the air-sea carbon flux stemming from regional imbalances and riverine/burial-driven fluxes is also provided above. (d) Partitioning of the integrated external sources and sinks of carbon (shaded) and Alk (hatched). The negative impact of OM burial on Alk is attributed to the release of ammonium when OM is remineralized at the seafloor rather than buried. Detailed descriptions of (c) and (d) can be found in Supplementary S1 and S2.

https://doi.org/10.5194/egusphere-2025-523
Preprint. Discussion started: 13 February 2025
© Author(s) 2025. CC BY 4.0 License.

Regions characterized by carbon-rich deep-water upwellings, such as equatorial and southern ocean upwelling zones, tend to show carbon outgassing. Conversely, poleward heat transport within the ocean, exemplified by western boundary currents like the Gulf Stream, promotes carbon absorption as surface waters cool. Consequently, the outcome is a pronounced meridional air-sea carbon flux gradient, with ingassing in the northern hemisphere ($+0.57$ PgC yr^{-1}), outgassing in the inter-tropical zone (-0.91 PgC yr^{-1}), and minimal outgassing in the southern hemisphere (-0.06 PgC yr^{-1}), primarily due to the impact of southern ocean upwelling between 45-65°S (Fig. 4b,c). The inter-hemispheric air-sea carbon flux gradient (G; Sect. 2.1.3) is $+0.51$ PgC yr^{-1}, while the inter-hemispheric transport of carbon and Alk (T^{C} and T^{Alk}; Sect. 2.1.3) amounts to -0.35 PgC yr^{-1} and -0.07 PgC yr^{-1}, respectively (see Fig. B3a).

The air-sea carbon flux can be subsequently decomposed into a component associated with the functioning of the ocean carbon pumps and a component associated with riverine and burial fluxes (Sect. 2.2.2). More specifically, we use the simulation without riverine and burial fluxes (norivbur) to isolate the distribution of air-sea carbon fluxes associated with the internal functioning of the ocean carbon pumps. Indeed, regional air-sea carbon fluxes are primarily influenced by these pumps, which establish and sustain vertical and horizontal carbon gradients within the ocean (e.g. Sarmiento and Gruber, 2006; Murnane et al., 1999; Aumont et al., 2001; Resplandy et al., 2018). Thus, both the physical pump (involving ocean circulation and air-sea carbon exchange) and the biological pump (comprising processes like production, export, and the remineralization/dissolution of OM and $CaCO_3$) play pivotal roles in elucidating the overall distribution of the air-sea carbon flux. These air-sea carbon fluxes exhibit significant ingassing in the northern hemisphere (+0.67 PgC yr^{-1}) and outgassing in the inter-tropical zone (-0.79 PgC yr^{-1}), with minimal ingassing in the southern hemisphere (+0.16 PgC yr^{-1}; see Table B1). Overall, the air-sea carbon flux associated with the oceanic carbon pumps is expected to be net-zero when integrated at the global scale, although norivbur shows a small residual component (+0.05 PgC yr^{-1}; see Fig.B3a). This residual component is attributed to a residual carbon budget imbalance due to internal ocean processes (see Appendix B1.3).

Finally, by taking the difference between our standard simulation and the simulation without riverine and burial fluxes (std minus norivbur), we isolate the component of interest, i.e. that induced by riverine and burial fluxes (Sect. 2.2.2). This riverine/burial-driven air-sea carbon flux results in a net global outgassing of 0.31 PgC yr^{-1}, distributed among the northern, inter-tropical, and southern regions as follows: 0.10, 0.12, and 0.10 PgC yr^{-1} (Fig. 4c).

3.2 The global riverine/burial-driven air-sea carbon flux

3.2.1 Role of sediment burial fluxes

At global scale, the riverine carbon flux in the standard simulation ($+0.52$ PgC yr^{-1}) is insufficient to fully account for the air-sea carbon outgassing (0.27 PgC yr^{-1}) alone (Fig. 4d and 5a). Indeed, it is necessary to consider carbon fluxes associated with OM and $CaCO_3$ burial (amounting to -0.17 and -0.04 PgC yr^{-1}, respectively; Fig. 2d and see Fig. B3a), which lessen the air-sea carbon outgassing to 0.31 PgC yr^{-1}.

The importance of burial fluxes in driving the riverine/burial-driven air-sea carbon flux is furthermore exemplified by our set of sensitivity simulations (Fig. 5a,b). Increasing the river input by a factor of 1.5 (riv1p5), drives an increase in carbon

https://doi.org/10.5194/egusphere-2025-523
Preprint. Discussion started: 13 February 2025
© Author(s) 2025. CC BY 4.0 License.

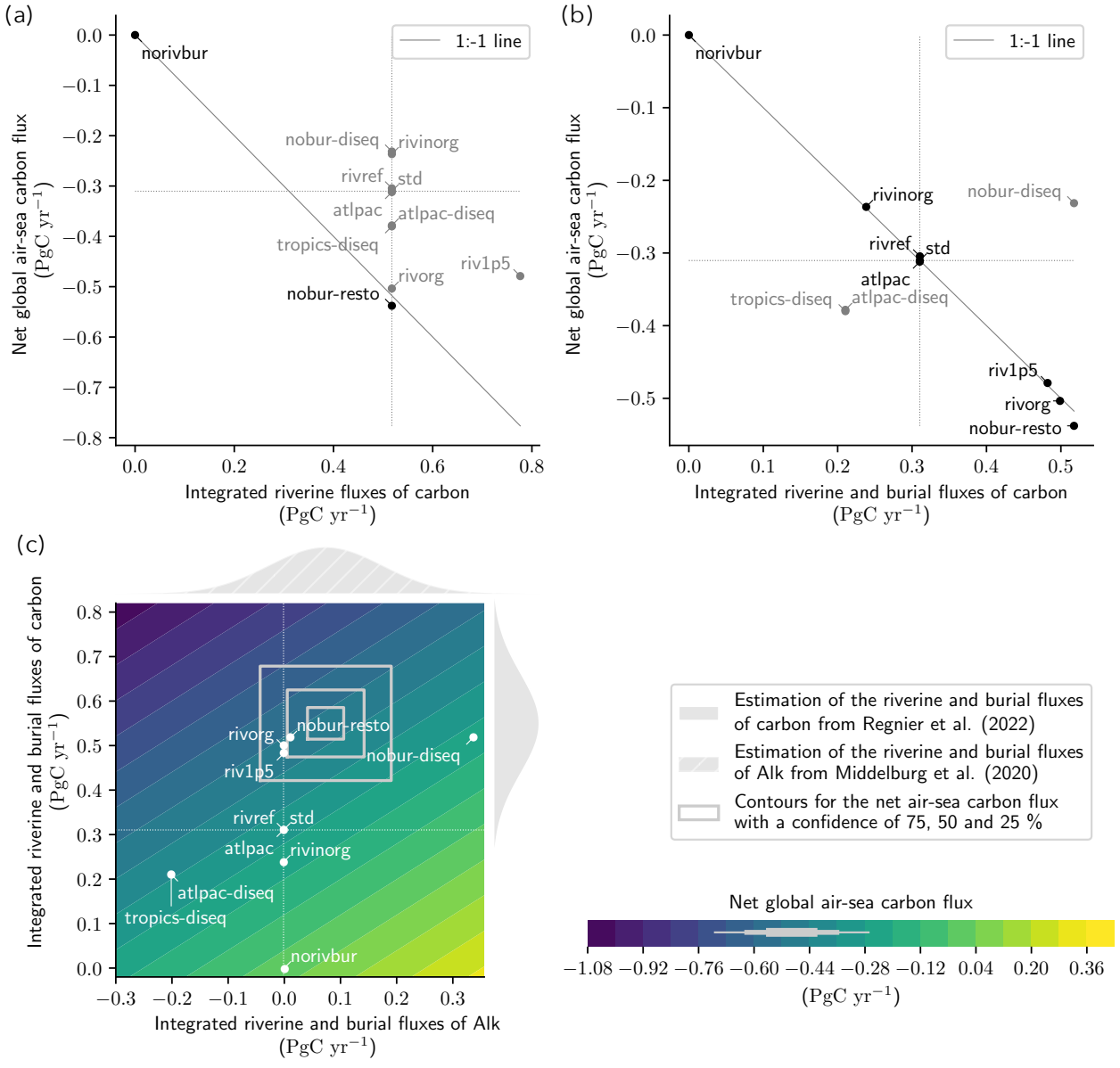

Figure 5. The role of riverine and burial fluxes of carbon and Alk in determining the pre-industrial air-sea carbon flux. (*continued*)

https://doi.org/10.5194/egusphere-2025-523
Preprint. Discussion started: 13 February 2025
© Author(s) 2025. CC BY 4.0 License.

Figure 5. (*continued*). (a, b) Comparison between the net global air-sea carbon flux[a] and (a) the integrated riverine fluxes of carbon, or (b) the integrated riverine and burial fluxes of carbon. When the net air-sea carbon flux balances the considered external fluxes (on the 1:1 line), simulation names are indicated in black. This applies to (a) simulations that do not account for burial and maintain Alk inventory at equilibrium (norivbur and nobur-resto), and (b) all simulations maintaining Alk inventory at equilibrium (excluding nobur-diseq, atlpac-diseq, and tropics-diseq). (c) Theoretical framework that accounts for Alk and carbon budgets to reconstruct the net air-sea carbon flux. The net air-sea carbon flux (filled contours) is determined by multiplying the integrated riverine and burial fluxes of Alk (x-axis) by Q_{inv} and then subtracting the integrated riverine and burial fluxes of carbon (y-axis). The deviation of the net air-sea carbon flux from this relationship in the NEMO-PISCES sensitivity simulations is small (less than $0.01\ \mathrm{PgC\ yr^{-1}}$ for all, except nobur-resto: less than $0.03\ \mathrm{PgC\ yr^{-1}}$). Simulations with a global Alk inventory at equilibrium align with the zero x-axis line. The most recent carbon and Alk budgets (Table 3) provide estimates of riverine and burial fluxes of carbon[b] and Alk[c], as shown at the top and on the right in grey. The net air-sea carbon flux reconstructed from these flux estimates are indicated as grey rectangles, with confidence intervals at 75 %, 50 %, and 25 %, and projected on the color bar.

[a]The net air-sea carbon flux of the NEMO-PISCES sensitivity simulations was adjusted for their respective residual carbon budget imbalances (see Appendix B1.3).

[b]This distribution also includes fluxes from groundwater discharge.

[c]This distribution also includes fluxes from anaerobic processes, groundwater discharge, and reverse weathering.

outgassing by 0.17 PgC yr^{-1}, which is only partly consistent with the increase in riverine carbon discharge ($+0.26$ PgC yr^{-1}; see Fig. B3b). This discrepancy arises because a portion (0.09 PgC yr^{-1}) of the additional carbon is sequestered in the form of $CaCO_3$ to maintain equilibrium in the global Alk inventory. Similarly, considering that riverine discharge consists exclusively of either organic or inorganic forms (rivorg and rivinorg), the magnitude of the river carbon input remains unaffected. However, the air-sea carbon ougassing is impacted (reaching 0.47 and 0.20 PgC yr^{-1}, respectively; see Table B1), primarily due to the associated decrease (increase) in the Alk riverine discharge relative to std (-0.38 and $+0.14$ PgC yr^{-1}, respectively; see Fig. B3b), which is accompanied by a corresponding reduction (increase) in $CaCO_3$ carbon burial relative to std ($+0.19$ and -0.07 PgC yr^{-1}, respectively). This underscores the significance of considering $CaCO_3$ burial when constructing the ocean carbon budget, especially when evaluating the net air-sea carbon flux.

The total carbon outgassing obtained from a simple carbon budget only holds however for our simulations in which the global Alk inventory is in equilibrium (Fig. 5b; Sect. 2.1.1), balancing the Alk input from rivers with the burial of $CaCO_3$ (Fig. 4d). When the global Alk inventory is not in equilibrium, it becomes necessary to consider the Alk budget in addition to the carbon budget to assess the riverine/burial-driven air-sea carbon flux (Sect. 2.1.1).

3.2.2 Impact of an imbalanced alkalinity budget

The possibility of an alkalinity budget not being in equilibrium during the pre-industrial era has been hypothesized several times in the past three decades (e.g. Milliman, 1993; Middelburg et al., 2020; Cartapanis et al., 2018; Boudreau et al., 2018). If this is the case, such a disequilibrium would have implications on the pre-industrial air-sea carbon flux (Methods). Two of our sensitivity simulations enable assessment of the implications of such a global Alk inventory disequilibrium. First, in atlpac-diseq, we introduced additional $CaCO_3$ burial in the deep Atlantic to better represent what is known from actual reconstructions

https://doi.org/10.5194/egusphere-2025-523
Preprint. Discussion started: 13 February 2025
© Author(s) 2025. CC BY 4.0 License.

of sediment types. Second, in tropics-diseq, we increased $CaCO_3$ burial in the shallow tropics to account for accumulation by coral reefs (tropics-diseq; Cartapanis et al., 2018).

In both simulations, the additional $CaCO_3$ burial drives additional carbon outgassing when compared to the std simulation. This may appear counter-intuitive when relying on a simple carbon budget, since these two simulations prescribed additional carbon removal from the ocean (to the sediment) and resulted in enhanced carbon loss at the air-sea interface (Fig. 5b). The extra $CaCO_3$ burial not only acts as an additional carbon sink for the ocean relative to std (0.10 PgC yr^{-1}; see Fig. B3b) but, due to the induced carbon:Alk imbalance (Sect. 2.1.2), it also leads to an increased carbon outgassing at equilibrium by 0.07 PgC yr^{-1} in both simulations relative to std. As a result, the disequilibrium in ocean carbon inventory relative to std (-0.16 PgC yr^{-1}) is even greater in absolute term than the extra $CaCO_3$ burial (0.10 PgC yr^{-1}), due to the associated outgassing (see Fig. B3b).

When the global Alk inventory is in disequilibrium, the air-sea carbon flux is no longer solely determined by the riverine and burial fluxes of carbon but also by the carbon:Alk imbalance induced by these fluxes relative to the equilibrium ratio with the atmospheric CO_2 concentration (Q_{inv}; Sect. 2.1.2). In such cases, the net air-sea carbon flux ($F^{\mathrm{C,\ air-sea}}$) can be expressed as the product of the integrated riverine and burial fluxes of Alk (F^{Alk}) multiplied by Q_{inv}, minus the integrated riverine and burial fluxes of carbon ($F^{\mathrm{C,\ bur./riv.}}$):

$$F^{\mathrm{C,\ air-sea}} = \underbrace{Q_{\mathrm{inv}} \cdot \overbrace{F^{\mathrm{Alk}}}^{D^{\mathrm{Alk}}}}_{D^{\mathrm{C}}} - F^{\mathrm{C,\ bur./riv.}}, \tag{22}$$

where D^{C} and D^{Alk} represent the global carbon and Alk inventory disequilibria. This underscores the significance of the global Alk inventory in estimating the pre-industrial air-sea carbon flux and, consequently, the importance of assumptions made regarding Alk equilibrium.

Specifically, we emphasize that with a global Alk inventory disequilibrium, the ocean can maintain an equilibrium with the atmospheric CO_2 concentration, resulting in a nearly constant air-sea carbon flux (Fig. B1) but a global carbon inventory disequilibrium (Fig. 5b). When the global Alk inventory is in equilibrium ($F^{\mathrm{Alk}} = 0$), a direct relationship between the riverine and burial fluxes of carbon and the net air-sea carbon flux becomes evident ($F^{\mathrm{C,\ air-sea}} = -F^{\mathrm{C,\ bur./riv.}}$).

3.2.3 A new estimate of the global riverine/burial-driven air-sea carbon flux

Using the theoretical framework introduced in this manuscript and literature-based estimates of riverine/burial fluxes of carbon and Alk, based on the most recent carbon and Alk budgets, we derive, from Eq. 22, a pre-industrial riverine/burial-driven air-sea carbon flux estimate of -0.49 $[-0.34; -0.70]$ PgC yr^{-1} (Table 3 and Fig. 5c). This pre-industrial riverine/burial-driven air-sea carbon flux is associated to carbon and Alk inventory disequilibria of 0.06 $[-0.05; 0.11]$ PgC yr^{-1} and 0.07 $[-0.06; 0.14]$ PgC yr^{-1}, respectively (see Fig. B4). This estimate is based on an integrated external flux of 0.55 $[0.45; 0.65]$ PgC yr^{-1} for carbon and 0.07 $[-0.06; 0.14]$ PgC yr^{-1} for Alk.

This estimate of -0.49 $[-0.34; -0.70]$ PgC yr^{-1} represents a downward revision of the latest riverine/burial-driven air-sea carbon flux estimate of -0.65 ± 0.30 PgC yr^{-1} currently used in the GCB (Friedlingstein et al., 2024) and based on an in-depth review of the land-to-ocean continuum of the global carbon cycle Regnier et al. (2022). Utilizing our value to estimate

https://doi.org/10.5194/egusphere-2025-523
Preprint. Discussion started: 13 February 2025
© Author(s) 2025. CC BY 4.0 License.

Table 3. Literature-based estimates of riverine/burial fluxes of carbon and Alk, from the most recent carbon and Alk budgets (Sect. 2.3 and see Fig. B7), including the calculation of the corresponding air-sea carbon flux, as well as carbon and Alk content disequilibria. The values are presented in petagrams of carbon per year. Values in brackets represent the uncertainty or extreme range, while the bold value indicates the best estimate or average. The intervals are arranged with the smallest absolute value first, except when both positive and negative values are present in the range.

Type of sources/sinks	Carbon flux (from Regnier et al., 2022)	Alk flux (from Middelburg et al., 2020)	Associated air-sea carbon flux ($Q_{\mathrm{inv}} \cdot F^{\mathrm{Alk}} - F^{\mathrm{C}}$)	Associated DIC disequilibrium ($Q_{\mathrm{inv}} \cdot F^{\mathrm{Alk}}$)	Associated Alk disequilibrium (F^{Alk})
Riverine discharge[a]	[0.650; 1.150]	[0.578; 0.929]	[-0.189; -0.410]	[0.461; 0.740]	[0.578, 0.929]
	0.900	0.756	-0.297	0.603	0.756
OM burial[b]	[-0.059; -0.155]	[0.014; 0.037]	[0.070; 0.184]	[0.011; 0.029]	[0.014; 0.037]
	-0.107	0.024	0.126	0.019	0.024
$CaCO_3$ burial	[-0.141; -0.345]	[-0.648; -0.828]	[-0.315; -0.375]	[-0.516; -0.660]	[-0.648; -0.828]
	-0.243	-0.708	-0.321	-0.564	-0.708
Total	[0.450; 0.650]	[-0.056; 0.138]	[-0.340; -0.695]	[-0.045; 0.110]	[-0.056; 0.138]
	0.550	**0.072**	**-0.493**	**0.057**	**0.072**

[a]Including fluxes from groundwater discharge and anaerobic processes.
[b]Including fluxes from reverse weathering.

anthropogenic carbon uptake in the ocean from pCO_2-based estimates would reduce the overall discrepancy between these observation-based estimates and model values by 0.16 PgC yr^{-1} over the entire period considered, thereby mitigating the current offset (Friedlingstein et al., 2024).

The discrepancy between our reassessment of riverine/burial-driven outgassing and the value currently used in the GCB underscores the crucial importance of clearly defining ocean boundary conditions and the pressing need to develop a combined and consistent carbon and Alk budget for the ocean to achieve a robust estimate. Part of this discrepancy arises because atmospheric carbon uptake by continental shelves (0.10 PgC yr^{-1} Regnier et al., 2022) is fully integrated into our net pre-industrial riverine/burial-driven air-sea carbon flux as we also consider OM and $CaCO_3$ burial in these regions, reducing this flux by 0.10 PgC yr^{-1}. The remaining reduction of 0.06 PgC yr^{-1} is linked to a slight imbalance in the global Alk inventory (0.07 PgC yr^{-1} Middelburg et al., 2020). However, the current inconsistency between the independently developed carbon and Alk budgets makes our estimate unreliable. If the burial flux of CaCO for carbon (Middelburg et al., 2020) is aligned with that for Alk (+0.22 PgC yr^{-1}; Table 3), the outgassing would decrease by an additional 0.18 PgC yr^{-1}. Conversely, if the burial flux of $CaCO_3$ for Alk (Middelburg et al., 2020) is aligned with that for carbon (-0.11 PgC yr^{-1}; Table 3), the outgassing would also drop, in this case by 0.11 PgC yr^{-1}, further reducing the current offset (Friedlingstein et al., 2024). Thus, it is essential to establish a combined and consistent carbon and Alk budget to confidently reassess this pre-industrial outgassing within the theoretical framework presented here.

https://doi.org/10.5194/egusphere-2025-523
Preprint. Discussion started: 13 February 2025
© Author(s) 2025. CC BY 4.0 License.

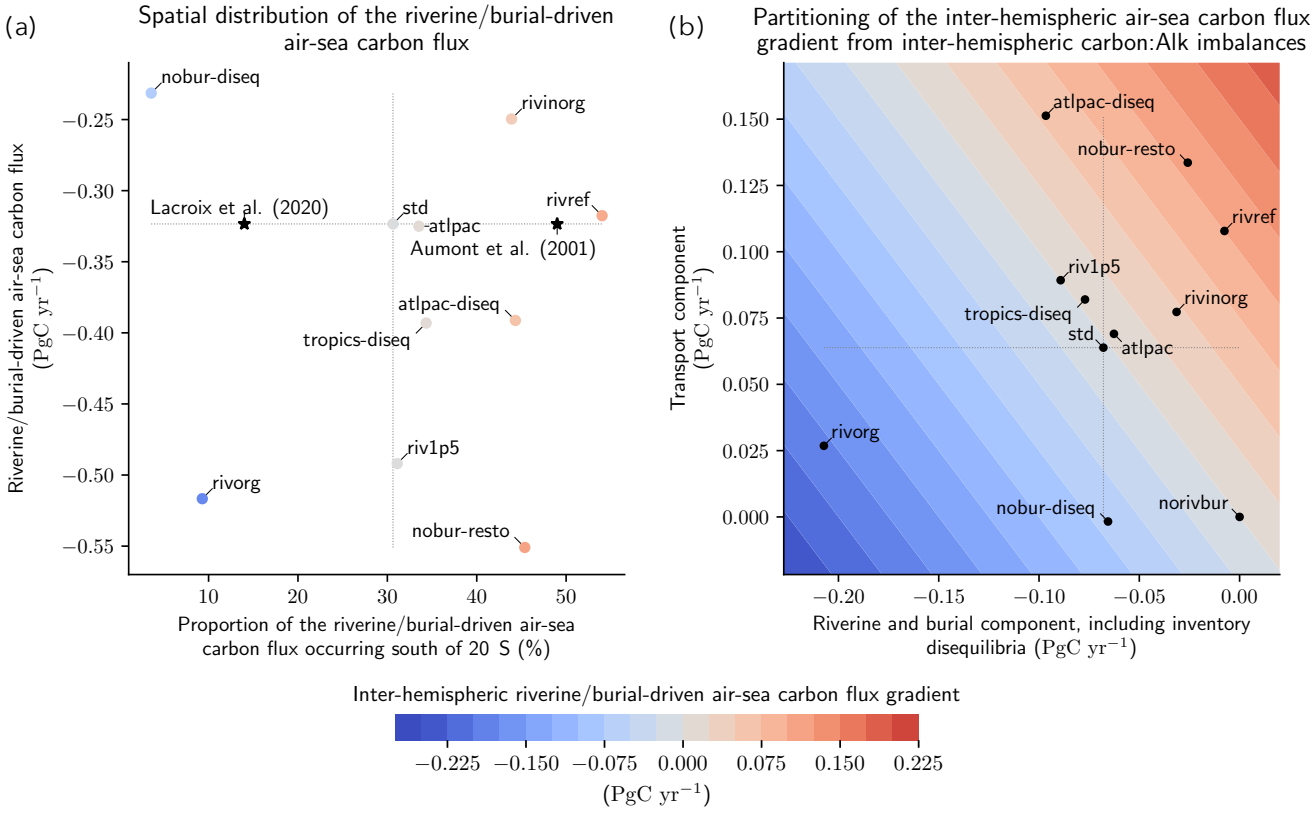

Figure 6. Distribution of the riverine/burial-driven air-sea carbon flux and its key drivers. (a) Comparison between the riverine/burial-driven air-sea carbon flux (y-axis, PgC yr^{-1}), the fraction of this flux occurring south of 20°S (x-axis, %) and its interhemispheric gradient (color dots, PgC yr^{-1}). The fraction of this flux occurring south of 20°S is also shown for Aumont et al. (2001) and Lacroix et al. (2020) (black stars), assuming the same riverine/burial-driven air-sea carbon flux as our standard simulation (std). (b) Inter-hemispheric gradient of the riverine/burial-driven air-sea carbon flux (filled contours) and its two components, from carbon:Alk imbalances (Sect. 2.1.2 and 2.1.3). One component (x-axis) is associated with the inter-hemispheric gradient of air-sea carbon flux driven by northern and southern carbon:Alk imbalances (and inventory disequilibria), while the other component (y-axis) corresponds to the inter-hemispheric gradient of air-sea carbon flux associated to the inter-hemispheric transport of the carbon:Alk imbalance (Eq. 19 and see Fig. B5). The deviation in the simulated inter-hemispheric gradient in NEMO-PISCES sensitivity simulations as compared to the reconstructed ones using the two components is minimal (< 0.01 PgC yr^{-1}, not shown).

3.3 The regional distribution of the riverine/burial-driven air-sea carbon flux

3.3.1 A highly contrasting regional distribution

385 The inter-hemispheric gradient of the pre-industrial air-sea carbon flux is primarily controlled by ocean interior processes and the functioning of the ocean carbon pumps. Specifically, in an ocean without any riverine and burial carbon fluxes (norivbur),

https://doi.org/10.5194/egusphere-2025-523
Preprint. Discussion started: 13 February 2025
© Author(s) 2025. CC BY 4.0 License.

the inter-hemispheric gradient amounts to $+0.51$ PgC yr^{-1} (see Fig. B3a). The biological pump contributes to carbon uptake in the northern hemisphere through surface biological activity and leads to carbon release in the southern hemisphere due to the upwelling of carbon-rich deep waters, as documented in previous studies (e.g. Murnane et al., 1999; Aumont et al., 2001; Resplandy et al., 2018). When subtracting the gradient estimated from simulation norivbur to all other sensitivity simulations, we find that only a fraction of the inter-hemispheric air-sea carbon flux gradient is accounted for by riverine and burial fluxes (ranging from -0.18 to $+0.11$ PgC yr^{-1} in our set of sensitivity simulations).

Our set of sensitivity simulations, exploring different assumptions on riverine and burial fluxes, encompass the uncertainty range of the inter-hemispheric gradient of the riverine/burial-driven air-sea carbon flux (Fig. 6a). The main point of contention around the inter-hemispheric gradient lies in the fraction of this flux occurring in the southern hemisphere, where most of the discrepancy in estimating the anthropogenic carbon flux between pCO_2-based and model estimates existed in GCBs (from 2018 to 2022; e.g. Hauck et al., 2020; Friedlingstein et al., 2022b) prior to being mostly transferred to the inter-tropical region (since 2023; e.g. Friedlingstein et al., 2023, 2024). In our simulations, the fraction of the flux occurring in the southern hemisphere ranges from less than 5 % (nobur-diseq) to more than 50 % (rivref). By comparison, it was estimated at 49 % (Aumont et al., 2001) and then 14 % (Lacroix et al., 2020) in the GCBs (Table YY and Fig. 7a), and even as low as 4 % in the literature (Jacobson et al., 2007). This is intriguing because one might expect that this distribution is primarily influenced by the strength of the meridional overturning circulation – and its effect on the southward transport of net riverine/burial carbon –, but our sensitivity simulations, with unchanged ocean dynamics, reveal highly contrasting distributions.

3.3.2 Influencing factors

There is no direct correlation between the magnitude of the riverine/burial-driven air-sea carbon flux and the proportion of this flux occurring south of 20°S (Fig. 6a). Notably, the substantial uncertainty on the refractory nature of organic riverine discharge (e.g., Aumont et al., 2001; Gruber et al., 2009) is demonstrated to result in a significant shift in the proportion of the riverine/burial-driven air-sea carbon flux occurring in the southern ocean (54 % in rivref vs. 31 % in std; Fig.6a), even though the total flux remains nearly the same. Conversely, when the riverine discharge is increased by 50 % (riv1p5), the distribution of the riverine/burial-driven air-sea carbon flux remains unchanged compared to std, while the total outgassing increases from 0.32 PgC yr^{-1} (std) to 0.49 PgC yr^{-1} (riv1p5; see Table B1).

The decoupling between the magnitude of the net riverine/burial-driven air-sea carbon flux and its inter-hemispheric gradient is primarily linked to the distribution, both horizontally and vertically, of the carbon:Alk imbalance resulting from riverine and burial fluxes. When an excess of $CaCO_3$ burial is considered at the bottom of the Atlantic (primarily in the northern hemisphere; atlpac-diseq), the resulting impact of the carbon:Alk imbalance on the riverine/burial-driven air-sea carbon flux occurs remotely, in the southern hemisphere, due to the meridional overturning circulation. This results in a relative outgassing compared to std (-0.07 PgC yr^{-1}), and an increase in the inter-hemispheric riverine/burial-driven air-sea carbon flux gradient ($+0.07$ PgC yr^{-1}; see Fig. B3b). On the contrary, when the surplus of $CaCO_3$ burial is in the shallow tropics (tropics-diseq), the riverine/burial-driven air-sea carbon flux anomaly compared to std is equivalent to the one reported for atlpac-diseq, but the inter-hemispheric gradient is this time nearly not impacted relative to std ($+0.01$ PgC yr^{-1}) since the flux anomaly is

https://doi.org/10.5194/egusphere-2025-523
Preprint. Discussion started: 13 February 2025
© Author(s) 2025. CC BY 4.0 License.

concentrated in the shallow tropics, primarily affecting the local air-sea carbon flux. Similarly, flux anomalies resulting from carbon:Alk imbalances with respect to the riverine fluxes tend to manifest locally, primarily in the northern hemisphere: (i) a fully organic riverine discharge leads to a relative outgassing compared to std (-0.19 PgC yr^{-1}), aligned with a decrease in the inter-hemispheric gradient (-0.18 PgC yr^{-1}); and (ii) a fully inorganic riverine discharge leads to a relative ingassing compared to std ($+0.07$ PgC yr^{-1}), aligned with an increase in the inter-hemispheric gradient ($+0.05$ PgC yr^{-1}; see Fig. B3b).

Nevertheless, it is crucial to have access to both the value of the riverine/burial-driven air-sea carbon flux and its spatial distribution to properly estimate the magnitude and distribution of the oceanic anthropogenic carbon uptake (e.g. Hauck et al., 2020; Friedlingstein et al., 2022b, 2024). It is possible to decompose the inter-hemispheric gradient of the riverine/burial-driven air-sea flux into a component associated with the inter-hemispheric transport of a carbon:Alk imbalance and a component associated with a carbon:Alk imbalance stemming from riverine and burial fluxes (including inventory disequilibria; Fig. 6b, Eq. 19, and Fig. B4). This demonstrates that when considering riverine and burial fluxes (std relative to norivbur), the component associated with these external fluxes (-0.07 PgC yr^{-1}) is offset by the transport-related component (+0.07 PgC yr^{-1}), resulting in a null inter-hemispheric riverine/burial-driven air-sea carbon flux gradient for std (Fig. 5b and Fig. 6b). In the case of a surplus of $CaCO_3$ burial in the deep Atlantic (atlpac-diseq), the increase in the inter-hemispheric riverine/burial-driven air-sea carbon flux gradient relative to std (+0.07 PgC yr^{-1}; see Fig. B3b) is primarily attributed to the transport of a carbon:Alk imbalance (Fig. 6b). Conversely, when the riverine discharge is entirely organic (rivorg), it is mostly the external flux component that causes the decrease in the inter-hemispheric air-sea carbon flux gradient relative to std (-0.18 PgC yr^{-1}; see Fig. B3b and Fig. 6b), and the same outcome occurs when the riverine discharge is entirely inorganic (rivinorg). This emphasizes that the spatial distribution of the carbon:Alk imbalance stemming from external fluxes, in conjunction with oceanic transport, plays a significant role in shaping the pre-industrial inter-hemispheric riverine/burial-driven air-sea carbon flux gradient.

3.3.3 A new estimate of the regional distribution of the riverine/burial-driven air-sea flux

The construction of a composite simulated estimate resulting from a linear combination of the NEMO-PISCES sensitivity simulations to align with the literature-based estimates for integrated fluxes of carbon and Alk (Fig. 7a; Sect. 2.3 and see Fig. B7) enables an estimation of the distribution of this riverine/burial-driven air-sea carbon outgassing (0.15 ± 0.13, 0.20 ± 0.10, and 0.16 ± 0.08 PgC yr^{-1} for the southern, inter-tropical, and northern regions, respectively; Fig. 7e). The uncertainty associated with these values is primarily linked to the uncertainties/extremes in literature-based estimates (see Fig. B4). Such a distribution implies that 29 % of the outgassing occurs in the southern region, 40 % in the inter-tropical region, and 31 % in the northern region. This represents an intermediate distribution compared to those used in the GCB over time, with recent values at 14 %, 64 %, and 22 % (Lacroix et al., 2020), and historical values at 49 %, 25 %, and 26 % (Aumont et al., 2001, Table 1). This would partially confirm the reduction in the discrepancy between pCO_2-based and model estimates in the southern region, while avoiding the introduction of a bias in the inter-tropical region, as it was noted in GCB 2023, (Friedlingstein et al., 2023) compared to previous GCBs (e.g. Friedlingstein et al., 2022b).

Furthermore, by summing the fluxes from the composite simulated estimate and the simulation without riverine and burial fluxes (norivbur), we obtain the total inter-hemispheric air-sea carbon flux gradient, which amounts to 0.50 ± 0.15 PgC yr^{-1}

https://doi.org/10.5194/egusphere-2025-523
Preprint. Discussion started: 13 February 2025
© Author(s) 2025. CC BY 4.0 License.

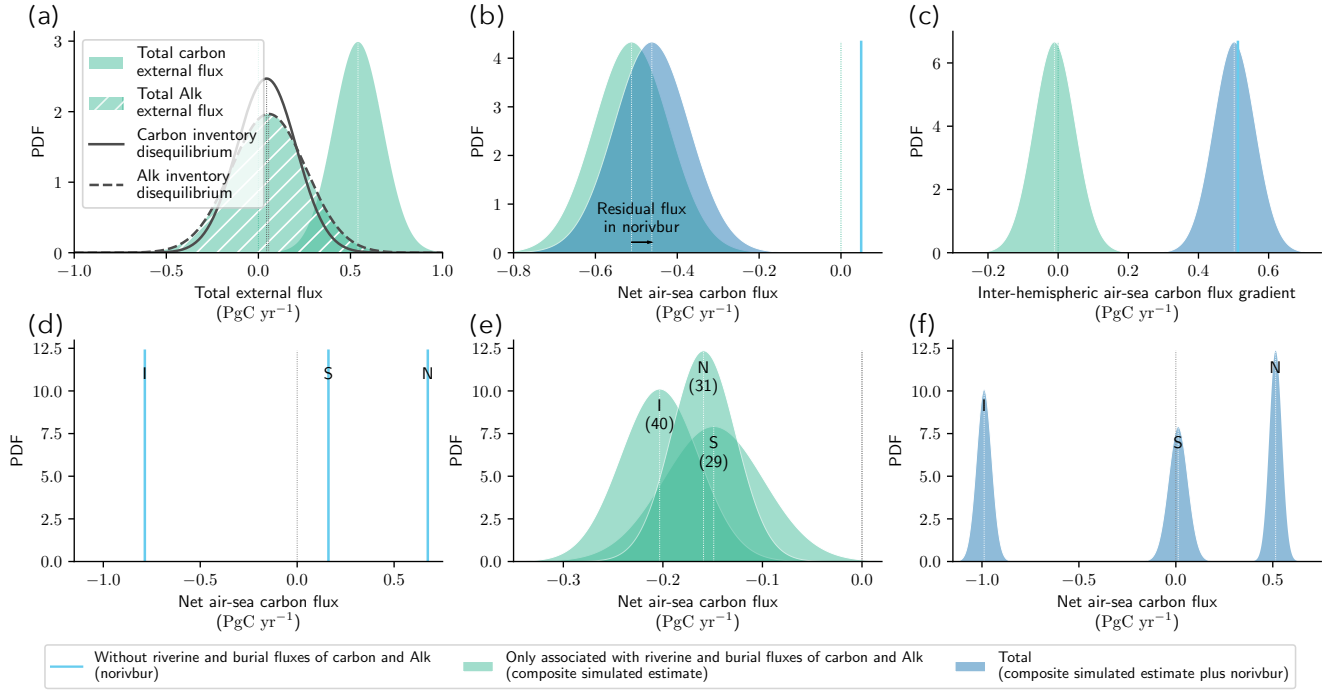

Figure 7. Description of the composite simulated estimate resulting from a linear combination of the NEMO-PISCES sensitivity simulations and literature-based estimates of riverine/burial fluxes of carbon and Alk (Sect. 2.3 and see Fig. B7). (a) PDF illustrating the total riverine and burial fluxes of carbon (shaded) and Alk (hatched) in the composite simulated estimate, along with the associated PDF for the resulting disequilibrium in carbon (solid) and Alk (dashed) content. (b,c) PDFs of the net air-sea carbon flux and the inter-hemispheric air-sea carbon flux gradient. Within each of these sub-panels, the PDF associated with no riverine and burial fluxes of carbon and Alk (norivbur; cyan line) is juxtaposed with the one corresponding to only riverine and burial fluxes of carbon and Alk (composite simulated estimate minus norivbur; aquamarine) to obtain the total value (composite simulated estimate; dark blue). Further details on the residual component where no riverine and burial fluxes are considered are explained in Appendix. B1.3. (d, e, f) The associated spatial distribution for the southern, inter-tropical, and northern regions: (d) without riverine and burial fluxes of carbon; (e) exclusively related to riverine and burial fluxes of carbon and Alk; and (f) the overall distribution. In (e), the percentage of each component is provided in brackets.

https://doi.org/10.5194/egusphere-2025-523
Preprint. Discussion started: 13 February 2025
© Author(s) 2025. CC BY 4.0 License.

(Fig. 7c). Notably, this value aligns with the inter-hemispheric CO_2 concentration gradient in the atmosphere between the South Pole and Mauna Loa during the pre-industrial era, which was historically assessed at $+0.82$ ppm (Keeling et al., 1989) and more recently reevaluated at $+0.55 \pm 0.15$ ppm (Resplandy et al., 2018) through interpolation of atmospheric CO_2 concentration measurements.

4 Conclusion and perspectives

The theoretical framework introduced here provides a novel perspective on the pre-industrial air-sea carbon flux through the lens of the alkalinity budget. Sensitivity simulations conducted with NEMO-PISCES underscore the utility and robustness of this framework in quantifying the riverine/burial-driven pre-industrial air-sea carbon flux using external carbon and alkalinity flux estimates. Specifically, based on the most recent literature-based estimates of carbon and alkalinity budgets (Regnier et al., 2022; Middelburg et al., 2020), we reassessed the pre-industrial outgassing flux associated with riverine and burial fluxes to be 0.49 $[0.34; 0.70]$ PgC yr^{-1}. This value is notably lower than the current estimate used in the GCB (0.65 ± 0.30 PgC yr^{-1} Friedlingstein et al., 2024). Importantly, this revised estimate reduces the discrepancy between observation-based and model-derived estimates of the anthropogenic ocean carbon sink by 0.16 PgC yr^{-1}. However, the revised flux estimate does not correct for any temporally varying biases (e.g. Hauck et al., 2023).

Additionally, the framework demonstrated its flexibility in integrating potential revisions of pre-industrial external carbon and alkalinity fluxes, as well as to consider changes in external fluxes resulting from human activities' impact, including both riverine and burial fluxes (e.g., Regnier et al., 2022). This adaptability is crucial, given the major uncertainties surrounding the pre-industrial alkalinity budget (e.g. Cartapanis et al., 2018) and the inconsistencies between current combined carbon and alkalinity budgets, which highlight an urgent need for a comprehensive review. Finally, the framework also emphasized the critical importance of precisely defining the boundary conditions of the oceanic domain at the coastal interface, within the land-to-ocean continuum, where multiple processes intersect (e.g. riverine discharge, and part of OM and $CaCO_3$ burial; Regnier et al., 2022; Gruber et al., 2023).

A practical framework was developed to estimate the distribution of the pre-industrial riverine/burial-driven air-sea carbon flux. Constructed as a linear combination of sensitivity simulations, this framework aligns with literature-based estimates of external carbon and alkalinity fluxes (Regnier et al., 2022; Middelburg et al., 2020). The reassessed distribution is 29 % in the southern region, 40 % in the inter-tropical region, and 31 % in the northern region, which is an intermediate distribution compared to those used in the GCB over time, with recent values at 14 %, 64 %, and 22 % (Lacroix et al., 2020), and historical values at 49 %, 25 %, and 26 % (Aumont et al., 2001).

As ocean circulation likely plays a pivotal role in partitioning these fluxes, applying this framework within a Global Ocean Biogeochemistry Model (GOBM) intercomparison exercise holds promise for better constraining the spatial distribution of this pre-industrial outgassing flux and enhancing confidence in the shared and adopted values in the GCB. Additionally, a better understanding of the intrinsic properties of these external fluxes is needed, such as whether the organic carbon brought by rivers is refractory or not (Aumont et al., 2001; Jacobson et al., 2007; Gruber et al., 2009). A more comprehensive characterization

https://doi.org/10.5194/egusphere-2025-523
Preprint. Discussion started: 13 February 2025
© Author(s) 2025. CC BY 4.0 License.

of external carbon and alkalinity fluxes remains a critical challenge for accurately constraining the magnitude and distribution of the riverine/burial-driven air-sea carbon flux.

Appendix A: Methods

A1 CMIP6 ESMs, GCB GOBMs, and associated air-sea carbon fluxes

We present an evaluation of the representation of the pre-industrial air-sea carbon flux in ESMs and GOBMS that participated in the CMIP6 exercise (Eyring et al., 2016) and the 2024 GCB exercise (Friedlingstein et al., 2024). This assessment offers valuable insights into the current state of the art regarding the modeling of this flux in the models utilized for intercomparison studies. To ensure comparability, we regridded the CMIP6 data to a regular 1°x1° grid using the distance-weighted average remapping method 'remapdis' provided by the Climate Data Operator (CDO). This step was taken as the data available from the 2024 GCB (Hauck et al., 2022) were already on a regular 1°x1° grid. However, it is important to note that this regridding process introduced a minor error in the integrated air-sea carbon flux values.

We assessed 15 CMIP6 ESMs from 12 different climate modelling centers (Eyring et al., 2016): CanESM5 (r1i1p2f1) and CanESM5-CanOE (r1i1p2f1) from CCCma, with two distinct marine biogeochemical models; CMCC-ESM2 (r1i1p1f1) from CMCC; CNRM-ESM2-1 (r1i1p1f2) from CNRM-CERFACS; ACCESS-ESM1-5 (r1i1p1f1) from CSIRO; IPSL-CM6A-LR (r1i1p1f1) from IPSL; MIROC-ES2L (r1i1p1f2) from MIROC; UKESM1-0-LL (r1i1p1f2) from MOHC; MPI-ESM1-2-LR (r1i1p1f1) and MPI-ESM1-2-HR (r1i1p1f1) from MPI-M, with two different resolutions; MRI-ESM2-0 (r1i2p1f1) from MRI, CESM2-WACCM (r1i1p1f1) from NCAR; NorESM2-LM (r1i1p1f1) from NCC; GFDL-CM4 (r1i1p1f1) and GFDL-ESM4 (r1i1p1f1) from NOAA-GFDL, with two distinct marine biogeochemical models. Only the air-sea CO_2 flux (positive donward, '$fgCO_2$' in kgC m^{-2} s^{-1}) of the pre-industrial control simulations was considered, from 1850 to 2100, and yearly averaged. Each ESM was weighted in the calculation of the CMIP6 mean, such that each modelling group has the same total contribution. We also assessed the 10 GOBMs used in the 2024 GCB exercise (Friedlingstein et al., 2024): NEMO3.6-PISCESv2-gas (CNRM), NEMO4.2-PISCES (IPSL), MPIOM-HAMOCC6, MRI-ESM2-3, ACCESS, MICOM-HAMOCC (NorESM-OC), MOM6-COBALT (Princeton), FESOM-2.1-REcoM3, NEMO-PlanckTOM12 and CESM-ETHZ). Once again, only the air-sea CO_2 flux (positive donward, '$fgCO_2$' in mol m^{-2} s^{-1}) of the control simulations (i.e. constant atmospheric CO_2, no climate change and variability) was considered, from 1959 to 2023, and yearly averaged. We found that the drift in the ESMs and GOBMs in the net air-sea carbon flux was consistently less than 0.10 PgC $(100\ yr)^{-1}$, and as such, it had negligible impact on the related results (see Fig. 2a and B6a).

A2 NEMO-PISCES sensitivity simulation configurations

We provide here additional details regarding the various configurations of the sensitivity simulations conducted using NEMO-PISCES (Table A1). In the standard configuration, the slight deviation (-0.02 PgC yr^{-1}) between Alk riverine discharge (+0.35 PgC yr^{-1}) and inorganic carbon riverine discharge (+0.37 PgC yr^{-1}) arises from the supply of inorganic nitrogen by

https://doi.org/10.5194/egusphere-2025-523
Preprint. Discussion started: 13 February 2025
© Author(s) 2025. CC BY 4.0 License.

rivers, presumed to be in the form of nitrate, which has a negative impact on Alk (Fig. B3). It is worth noting that the latitudinal distribution of riverine inputs is based on Ludwig et al. (1996) and may undergo revision in the future, particularly following Li et al. (2017), although the human imprint on these fluxes cannot be removed. Lastly, we emphasize that we did not evaluate the implications of partitioning riverine inputs between inorganic and organic components on biological production, and consequently, its effects on the air-sea carbon flux, as we only altered DIC and Alk in the various configurations. Finally, we accounted for atmospheric deposition in our sensitivity simulations, since atmospheric nitrogen deposition is considered a nitrate source, which impacts Alk. This has however a negligible effect, as does the dilution effect (see Supplementary S2).

The manuscript has been crafted to be accessible and comprehensible for both observationalists and modelers. However, the disequilibria mentioned for the carbon and Alk inventories manifest themselves in model outputs in the form of drifts. Furthermore, all the sensitivity simulations conducted also address modeling issues. In particular, a case that can be encountered in marine biogeochemistry models, both historically and even today, is the consideration, or lack thereof, of the OM and $CaCO_3$ burial, and the consequences this can have on the carbon flux, depending on whether the global Alk inventory is equilibrated through a global-scale Alk restoration scheme, or left in disequilibrium (nosed-resto, nosed-diseq; Planchat et al., 2023). Finally, the choice of the different configurations, and their resulting impact on the air-sea carbon flux, also serve as a reminder of the importance of carefully considering the global Alk inventory in models, and controlling its potential disequilibrium/drift according to desired hypotheses (e.g. global Alk inventory equilibrium or not).

From a practical standpoint, in NEMO-PISCES, $CaCO_3$ burial predominantly occurs in coastal areas (Fig. A1a), with limited differentiation in burial at depth between the Atlantic (less acidic) and Pacific (more acidic) regions (Sarmiento and Gruber, 2006; Cartapanis et al., 2018; Ridgwell and Zeebe, 2005, Fig. A1a). To address this limitation, we introduced the configuration 'atlpac-diseq' wherein we constrain extra $CaCO_3$ burial in the deep Atlantic while simulating extra $CaCO_3$ dissolution in the deep Pacific. This adjustment aims to enhance the representation of $CaCO_3$ burial while maintaining global Alk inventory equilibrium (Fig. A1b). Additionally, considering the possibility of a disequilibrium in the global Alk inventory during the pre-industrial era due to extra $CaCO_3$ burial at depth (Cartapanis et al., 2018), we created two configurations to account for this extra carbon burial (0.10 PgC yr^{-1}): (i) in the deep Atlantic (atlpac-diseq), and (ii) in the shallow tropical regions (tropics-diseq), simulating the accumulation of carbon by corals (Fig. A1b).

https://doi.org/10.5194/egusphere-2025-523
Preprint. Discussion started: 13 February 2025
© Author(s) 2025. CC BY 4.0 License.

Table A1. Summary of the sensitivity simulations led with NEMO-PISCES with their full description and characteristics (supplement to Table 2).

Configuration		Parametrization					
Simulation	Description	Alk inventory	Riverine discharge	OM burial	$CaCO_3$ burial	Atmospheric deposition	Net addition	Alk restoration
std	Standard	Equilibrium	X	X	Equilibrating the global Alk inventory	X	–	–
norivbur	No external fluxes of carbon and Alk, except air-sea carbon fluxes	Equilibrium	–	–	–	–	–	–
rivref	Refractory organic riverine discharge	Equilibrium	Alk and carbon from organic riverine discharge are spread all over the ocean	X	Equilibrating the global Alk inventory	X	–	–
rivorg	Fully organic riverine discharge	Equilibrium	For every mole of carbon discharged by rivers, Alk is discharged with the N : C ratio of organic carbon discharge	X	Equilibrating the global Alk inventory	X	–	–
rivinorg	Fully inorganic riverine discharge	Equilibrium	For every mole of carbon discharged by rivers, a mole of Alk is also discharged	X	Equilibrating the global Alk inventory	X	–	–
riv1p5	Riverine discharge of carbon and Alk multiplied by 1.5	Equilibrium	1.5 times the amount of carbon and Alk supplied in std	X	Equilibrating the global Alk inventory	X	–	–
nosed-resto	No OM and $CaCO_3$ burial, but restoration of the Alk content	Equilibrium	X	–	–	X	–	X
nosed-diseq	No OM and $CaCO_3$ burial	Disequilibrium	X	–	–	X	–	–
atlpac	Constrained balance of extra $CaCO_3$ burial/dissolution between the deep Atlantic/Pacific	Equilibrium	X	X	Equilibrating the global Alk inventory, without considering 'net addition'	X	Equivalent amount of carbon and Alk added/removed in the deep Pacific/Atlantic (0.10 PgC yr-1 of carbon and 0.20 PgC yr-1 of Alk)	–
atlpac-diseq	Constrained imbalance of extra $CaCO_3$ burial/dissolution between the deep Atlantic/Pacific (-0.10 PgC yr-1)	Disequilibrium	X	X	Equilibrating the global Alk inventory, without considering 'net addition'	X	Twice more carbon and Alk removed in the deep Atlantic compared to the deep Pacific (-0.20 PgC yr-1 relative to 0.10 PgC yr-1 of carbon, and -0.40 PgC yr-1 relative to 0.20 PgC yr-1 of Alk)	–
tropics-diseq	Constrained extra $CaCO_3$ burial in the shallow tropics (-0.10 PgC yr-1)	Disequilibrium	X	X	Equilibrating the global Alk inventory, without considering 'net addition'	X	Removal of carbon and Alk in the shallow tropics (-0.10 PgC yr-1 for carbon and -0.20 PgC yr-1 for Alk)	–

https://doi.org/10.5194/egusphere-2025-523
Preprint. Discussion started: 13 February 2025
© Author(s) 2025. CC BY 4.0 License.

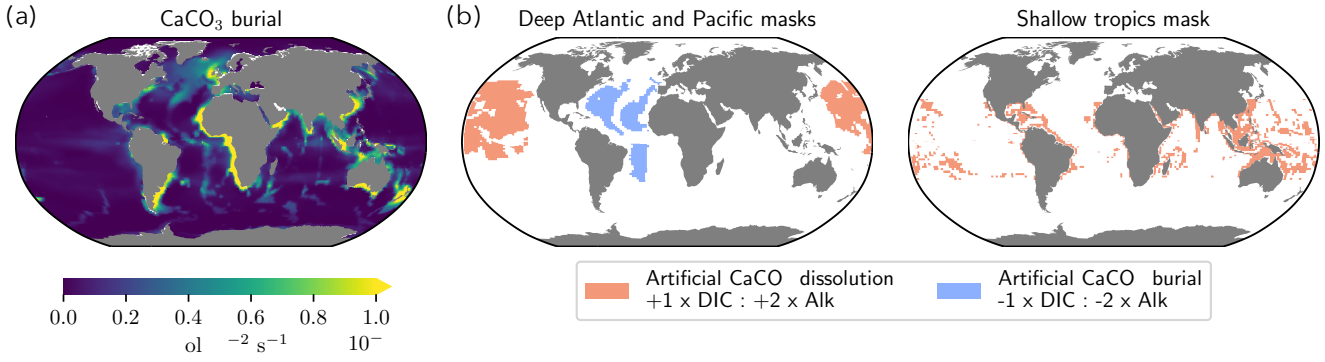

Figure A1. Towards a controlled adjustment of extra $CaCO_3$ burial/dissolution. (a) Map depicting $CaCO_3$ burial in the standard simulation (std). (b, c) Masks employed to drive (b) a balanced (atlpac) or an imbalanced (atlpac-diseq) additional $CaCO_3$ burial/dissolution between the deep Atlantic and Pacific, as well as (c) an extra $CaCO_3$ burial in the tropics. Red (blue) shading represents an addition (removal) of DIC and Alk in the grid cell at a 1:2 ratio. The grid cells considered for this addition/removal are located at 4750 m for the deep Atlantic and Pacific masks, and between 0 and 100 m for the tropics mask.

A3 The practical framework

We provide a schematic of the practical framework introduced in this manuscript (Sect. 2.3), which follows a four-step workflow to construct a composite simulation aligning with the most recent carbon and Alk budgets (Fig. A2).

A4 Ocean regions, and boundary conditions

The boundaries chosen to demarcate the southern, inter-tropical, and northern regions at 20°S and 20°N (see Fig. 4b, 3a, as well as Tables B1, B2, and B3) have indeed been previously employed in the literature (e.g., Aumont et al., 2001; Resplandy et al., 2018). These boundaries primarily align with physical features of the ocean, especially concerning air-sea carbon fluxes. It is in, or very close, to these latitudes that the air-sea carbon flux resulting from local imbalance reconciles with the simulated one (see Fig. 4c). By employing these boundaries, the air-sea carbon flux from regional carbon:Alk imbalances (see Sect. 2.1.2) closely matches the simulated values for each oceanic region (see Supplementary S1). This alignment deteriorates when the boundaries are shifted away from 20°S and 20°N. Consequently, we have opted for a consistent approach, maintaining the 20°S/N boundary to delineate distinct oceanic regions, despite the shift to 30°S/N boundaries in the GCB, primarily to correspond with terrestrial biomes (Friedlingstein et al., 2024). However, for potential use in the GCB, we share values of the spatial distribution with boundaries at 30°S/N in Table B3.

https://doi.org/10.5194/egusphere-2025-523
Preprint. Discussion started: 13 February 2025
© Author(s) 2025. CC BY 4.0 License.

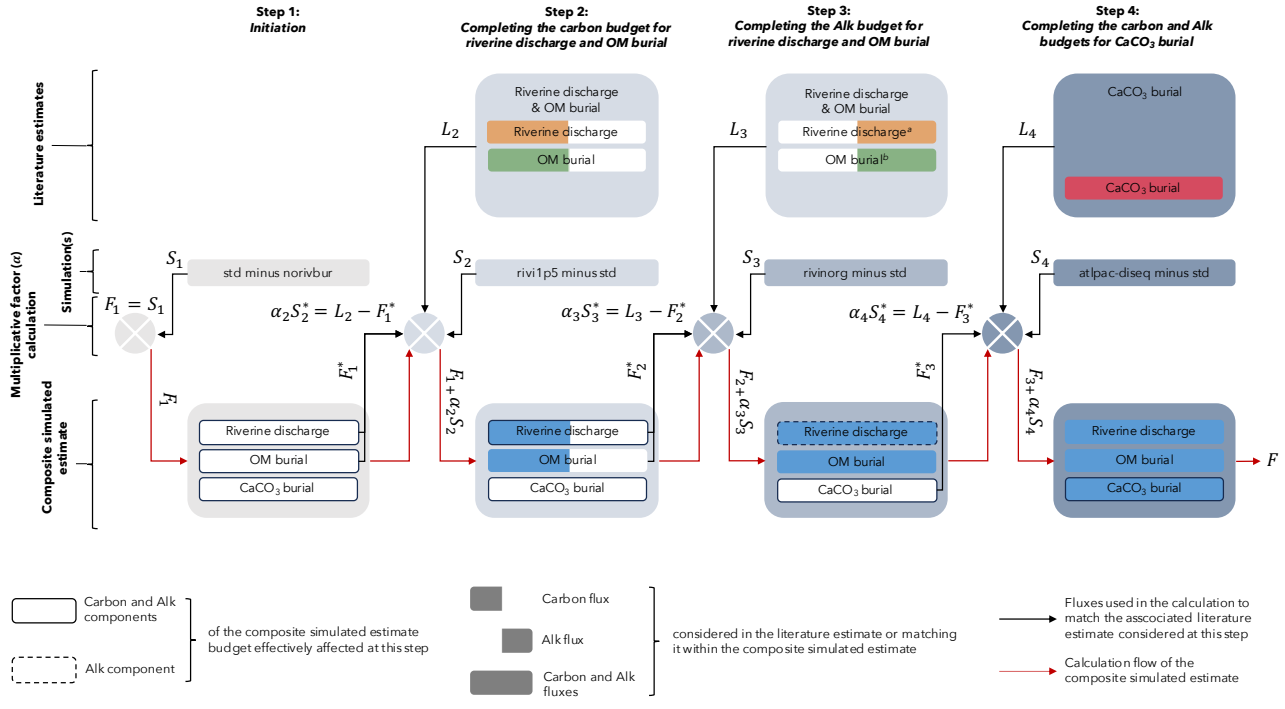

Figure A2. Schematic of the practical framework introduced in this manuscript. Four-step workflow to construct a composite simulated estimate of the riverine/burial-driven air-sea carbon flux from a linear combination of our sensitivity simulations to match the most recent carbon and Alk budgets (riverine discharge, OM burial, and $CaCO_3$ burial). An additional step, equivalent to Step 3 but not shown in this general workflow, was necessary to adjust the $CaCO_3$ burial of carbon in excess (Regnier et al., 2022), compared to the values accounted for Alk (Middelburg et al., 2020).

Appendix B: Results and discussion

B1 NEMO-PISCES sensitivity simulations

B1.1 Spin-up

We track here the evolution of the net air-sea carbon flux during the spin-up for all the NEMO-PISCES sensitivity simulations (Table A1 and Fig. B1a), which are initially branched to a simulation at quasi-steady state equivalent to our standard simulation (std). Two characteristic time-scales emerge (Fig. B1b): (i) a short-term equilibration over the first 50 yr, and (ii) a long-term equilibration beyond 50 yr. The short-term (long-term) equilibration primarily corresponds to the response of the surface (deep) ocean to the modifications associated with the configuration regarding the DIC and Alk external fluxes (Fig. B1c,d). Thus, for the simulation where we constrain extra $CaCO_3$ burial in the shallow tropics, only an equilibration of the surface ocean is generally needed, resulting in only a short-term equilibration. On the contrary, in the case where this extra $CaCO_3$ burial is constrained in the deep Atlantic, only an equilibration of the deep ocean is generally needed, resulting in only a long-term

https://doi.org/10.5194/egusphere-2025-523
Preprint. Discussion started: 13 February 2025
© Author(s) 2025. CC BY 4.0 License.

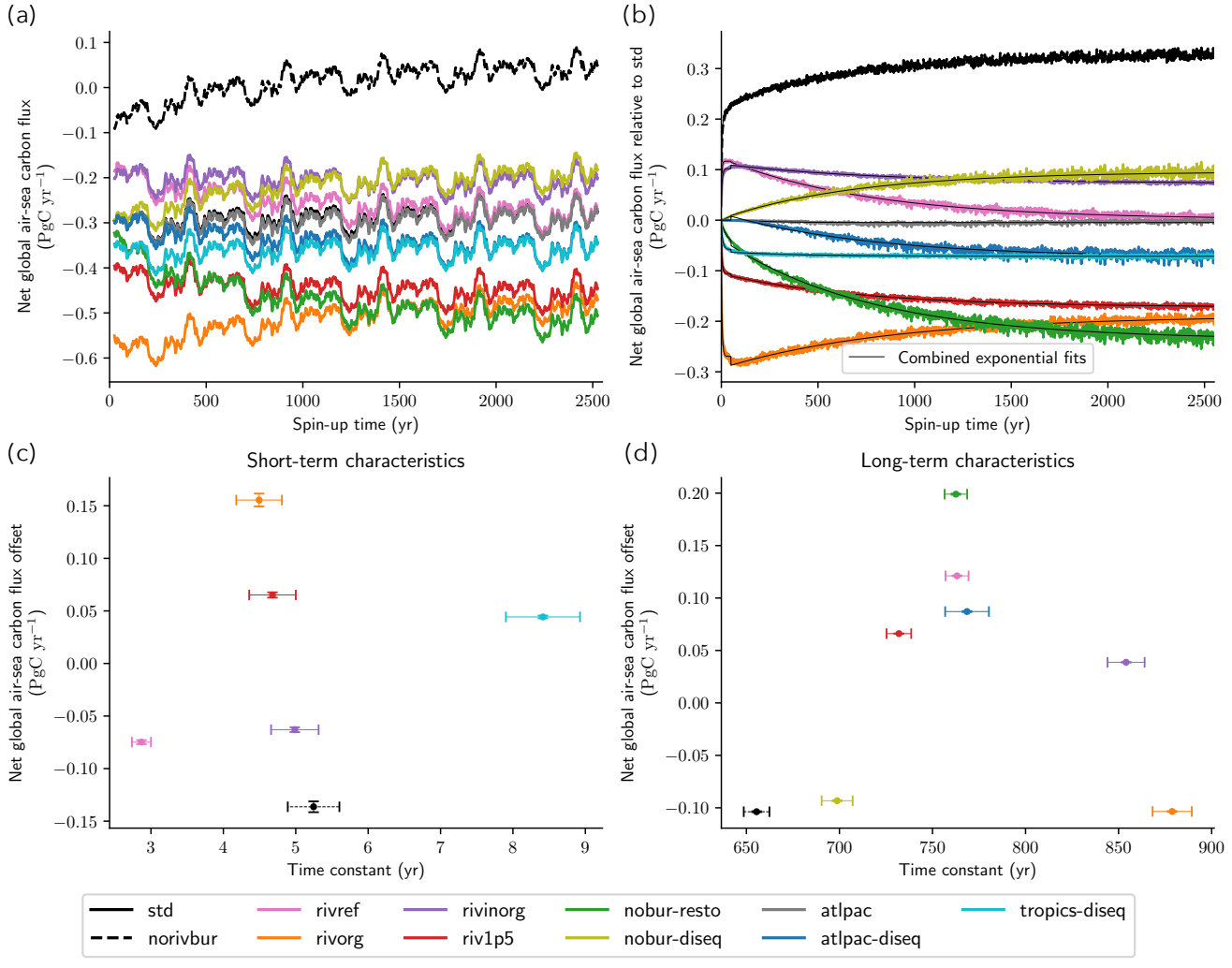

Figure B1. Spin-up of the NEMO-PISCES sensitivity simulations. (a) Time series of the net air-sea carbon flux with a 50-yr rolling mean throughout the 2550 yr of the simulations. (b) Same time series in relative to std and without smoothing. The thin black lines refer to the combined exponential fits ($y = \alpha \cdot e^{-\frac{t}{\tau}} + \beta$, where α is the net air-sea carbon flux offset, τ is the time constant, and β is the baseline; using the *curve_fit* function from the *scipy* python library): (i) one for the short-term considering the first 50 yr; and (ii) one for the long-term, considering the remaining 2500 yr. (c, d) for the short-term (c) and long-term (d) exponential fits, the net air-sea carbon flux offset (α) is displayed in function of the time constant (τ) with their associated uncertainties.

equilibration. Finally, in the case where riverine organic matter input is considered to be entirely refractory (rivref), a significant anomaly in external fluxes is induced at the surface compared to the standard simulation (std), as well as in the deep ocean because this organic carbon input is spread all over the ocean. This results in both short-term and long-term responses.

https://doi.org/10.5194/egusphere-2025-523
Preprint. Discussion started: 13 February 2025
© Author(s) 2025. CC BY 4.0 License.

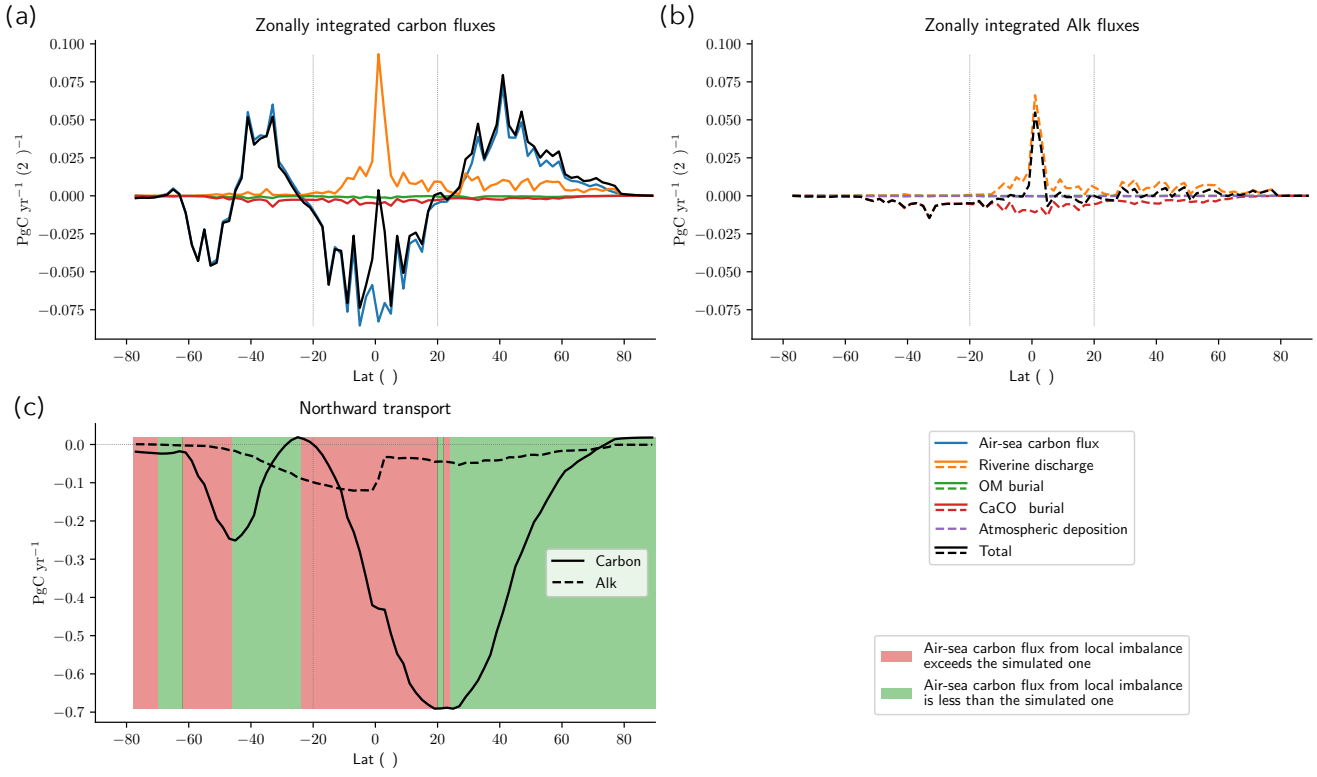

Figure B2. Description of the standard NEMO-PISCES simulation (std; continued from Fig. 2). Zonally integrated (a) carbon and (b) Alk fluxes in supplement to Fig. 2b. (c) Latitudinal distribution of the northward transport of carbon (solid) and Alk (dahsed). When the local imbalance exceeds (falls behind) the simulated air-sea carbon flux, the area in between is shaded in red (green).

B1.2 Standard simulation (std)

We provide additional details here regarding the standard simulation (std, Fig. B2) to offer points of comparison with historical modeling studies that have initiated research efforts on this pre-industrial carbon flux (Aumont et al., 2001; Murnane et al., 1999).

B1.3 Residual carbon budget imbalance

A minor imbalance in the carbon budget from external sources/sinks persists without any associated ocean carbon content disequilibrium in our sensitivity simulations. This discrepancy is particularly evident in the standard simulation (std; see 'Total' and 'Drift' in Fig. 4d) but is also observed in other simulations such as rivref, rivorg, rivinorg, riv1p5, atlpac, atlpac-diseq, and tropics-diseq (see Supplementary S2). To understand this counter-intuitive result initially, we must examine diazotrophic organisms, which produce OM without altering Alk. Let's imagine a thought experiment where the ocean contains external sources/sinks of carbon and Alk, such as riverine discharge and $CaCO_3$ burial, but maintains a global Alk inventory of zero.

https://doi.org/10.5194/egusphere-2025-523
Preprint. Discussion started: 13 February 2025
© Author(s) 2025. CC BY 4.0 License.

Then, the ocean carbon balance can be performed independently of Alk to infer the air-sea carbon flux at equilibrium (see Sect. 3.2.2). Now, let's introduce the production of OM by diazotrophic organisms into this ocean at equilibrium, assuming that all of it is buried. These organisms will consume carbon in the surface ocean and export it in the sediments without affecting Alk. This leads to a carbon sink in the ocean, which, when brought back to equilibrium, is counter-balanced by a positive air-sea carbon flux. Therefore, the imbalance in the carbon budget for std results from the OM burial produced by diazotrophs. In reality, the effect of diazotrophic organisms is more complex, as only a fraction of their OM is buried, and the rest is remineralized, leading to an increase in Alk. However, a similar effect on the air-sea carbon flux would be observed, albeit with a different magnitude. Since we could not determine the distribution of this induced air-sea carbon flux, we could not correct this slight imbalance in the carbon budget from external sources/sinks, except in Fig. 5, where only the total value of the air-sea carbon flux is considered, without its distribution. Please note that this unaccounted-for air-sea carbon flux stemming from external ocean carbon and Alk sources/sinks also contributes to the understanding of the slight discrepancy between the simulated air-sea carbon flux and the one resulting from global imbalance (e.g. $+0.04$ PgC yr^{-1} for std; see Fig. 4c and Fig. B3a).

Another type of imbalance in the carbon budget is evident in the simulation without external ocean source/sink (norivbur), accompanied by a disequilibrium in ocean carbon and Alk contents (see 'Total' and 'Drift' in Supplementary S2 and Fig. B3a). This imbalance arises from the representation of nitrogen reactions in NEMO-PISCES, which includes the restoration of nitrate content in the ocean. An imbalance between nitrification (decreasing Alk) and denitrification (increasing Alk) leads to an internal Alk disequilibrium (an imbalance stemming from N-reactions is also reported in COBALTv2 Stock et al., 2020). This is not compensated for by the strategy used to maintain the global Alk inventory, as $CaCO_3$ burial is not considered in this simulation (see Sect. 2.2). At equilibrium, this positive global Alk inventory disequilibrium (D'^{Alk}) results in an air-sea carbon flux ($F'^{\mathrm{C,\ air-sea}}$) and an ocean carbon content disequilibrium (D'^{C}) of the same magnitude: $F'^{\mathrm{C,air-sea}} = D'^{C} = Q_{\mathrm{inv}} \cdot D'^{\mathrm{Alk}}$ (see Fig. 3b and Sect. 3.2.2). Thus, the imbalance in the carbon budget for norivbur is associated with an air-sea carbon flux resulting from an internal Alk disequilibrium, also leading to a disequilibrium in ocean carbon content. As expected, this imbalance is almost equivalent in the simulation without burial and a global Alk inventory disequilibrium (nobur-diseq). Once again, as we were unable to access the distribution of this induced air-sea carbon flux, we could not correct this slight imbalance in the carbon budget from external sources/sinks, except in Fig. 5, where only the total value of the air-sea carbon flux is considered.

Very minor residual undesirable disturbances, such as disequilibria or slight inconsistencies in the budgets over the 50-year period considered, may persist due to the minor non-linearity occurring during the burial of $CaCO_3$ when the global Alk inventory is constrained to be equilibrated by the burial of $CaCO_3$. Additionally, the modeling scheme of the physical part of NEMO-PISCES induces a slight Alk disequilibrium and a slightly more pronounced carbon content disequilibrium (respectively -0.002 PgC yr^{-1} and $+0.01$ PgC yr^{-1} in std).

https://doi.org/10.5194/egusphere-2025-523
Preprint. Discussion started: 13 February 2025
© Author(s) 2025. CC BY 4.0 License.

Table B1. Comprehensive description of the net air-sea carbon flux in the NEMO-PISCES sensitivity simulations. The values provided in parentheses are expressed relative to the simulation without riverine and burial fluxes, representing the riverine/burial-driven air-sea carbon flux or carbon transport.

Simulation	Net air-sea carbon flux					Inter-hemispheric
	South (<20°S)	Inter-tropics (20°S - 20°N)	North (>20°N)	Total	Inter-hemispheric gradient (north - south)	transport of carbon
std	0.06 (-0.10)	-0.91 (-0.12)	0.57 (-0.10)	-0.27 (-0.32)	0.51 (-0.00)	-0.35 (-0.09)
norivbur	0.16	-0.79	0.67	0.05	0.51	-0.26
rivref	-0.01 (-0.17)	-0.86 (-0.08)	0.61 (-0.07)	-0.27 (-0.32)	0.62 (0.10)	-0.37 (-0.11)
rivorg	0.11 (-0.05)	-1.03 (-0.24)	0.45 (-0.23)	-0.47 (-0.52)	0.33 (-0.18)	-0.24 (0.02)
rivinorg	0.05 (-0.11)	-0.86 (-0.08)	0.61 (-0.06)	-0.20 (-0.25)	0.56 (0.05)	-0.38 (-0.12)
riv1p5	0.01 (-0.15)	-0.97 (-0.19)	0.52 (-0.15)	-0.44 (-0.49)	0.51 (0.00)	-0.40 (-0.15)
nobur-resto	-0.09 (-0.25)	-0.95 (-0.16)	0.54 (-0.14)	-0.50 (-0.55)	0.62 (0.11)	-0.40 (-0.14)
nobur-diseq	0.15 (-0.01)	-0.93 (-0.14)	0.59 (-0.08)	-0.18 (-0.23)	0.44 (-0.07)	-0.31 (-0.05)
atlpac	0.05 (-0.11)	-0.90 (-0.12)	0.57 (-0.10)	-0.28 (-0.33)	0.52 (0.01)	-0.36 (-0.10)
atlpac-diseq	-0.01 (-0.17)	-0.89 (-0.11)	0.57 (-0.11)	-0.34 (-0.39)	0.58 (0.06)	-0.36 (-0.11)
tropics-diseq	0.03 (-0.14)	-0.92 (-0.13)	0.55 (-0.13)	-0.34 (-0.39)	0.52 (0.01)	-0.35 (-0.09)

B1.4 NEMO-PISCES sensitivity simulation ensemble

We provide a comprehensive overview of the global-scale carbon and Alk budgets for all NEMO-PISCES sensitivity simulations (Fig. B3). Even more detailed information can be found in Supplementary S1 and S2 (https://doi.org/10.5281/zenodo.8421898). Finally, we also provide a comprehensive characterization of the air-sea carbon flux in the NEMO-PISCES sensitivity simulations, including both the total flux and the riverine/burial-driven component (Table B1).

B2 Literature review

Here, we provide a literature review on: (i) the evolution of the assessment and characterization of the air-sea carbon flux since the late 1990s (Table B2); and (ii) the evolution of the estimation and characterization of the riverine/burial-driven air-sea carbon flux in comparison with our composite simulated estimate (Table B3). We also provide the PDFs of the literature-based estimates for the ocean's external sources/sinks of carbon and Alk, derived from the most recent carbon and Alk budgets (Regnier et al., 2022; Middelburg et al., 2020), which were used to construct the composite simulated estimate (Fig. B4, see Table 3 as well as Sect. 2.3 and 3.3.3).

https://doi.org/10.5194/egusphere-2025-523
Preprint. Discussion started: 13 February 2025
© Author(s) 2025. CC BY 4.0 License.

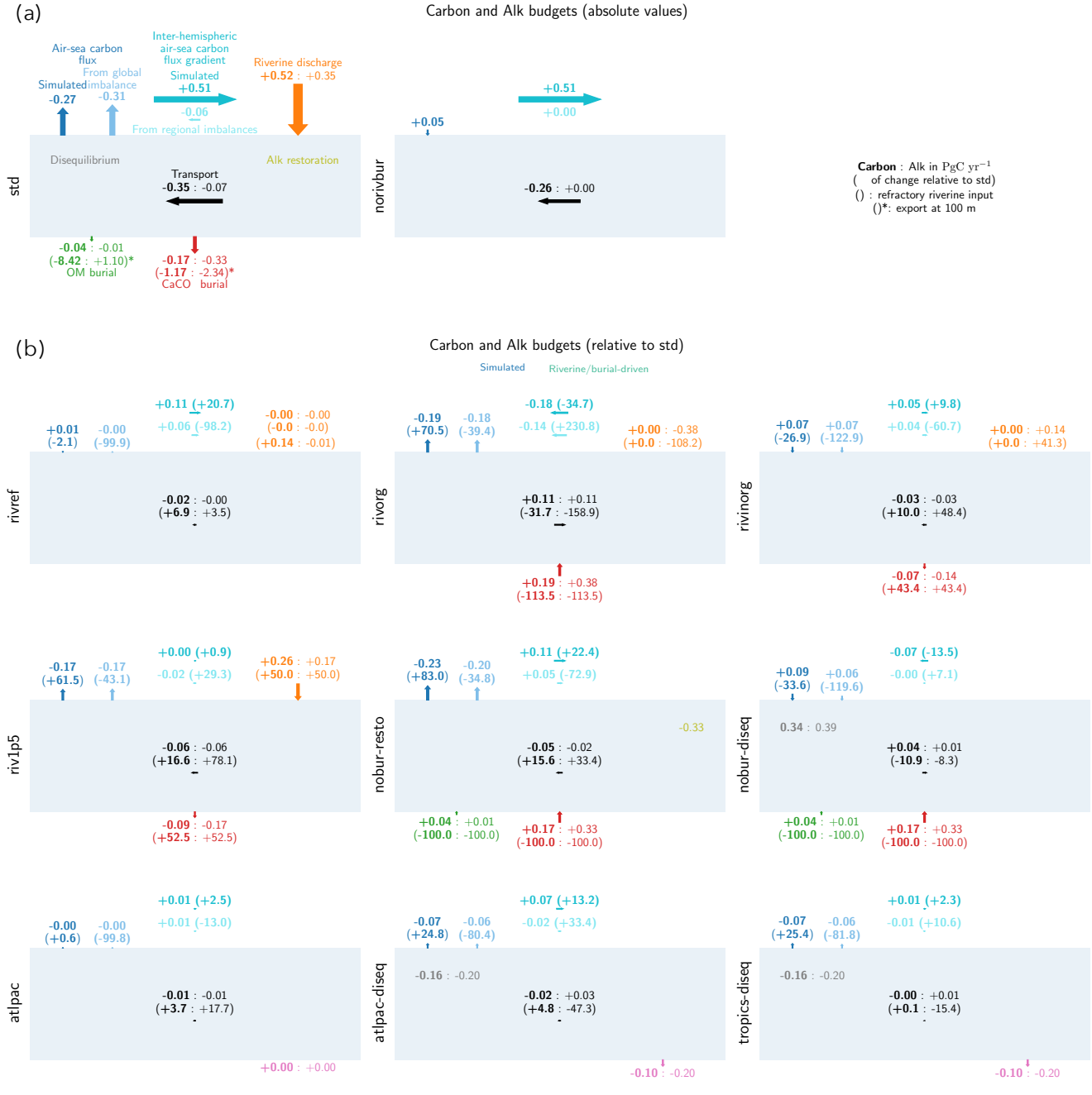

Figure B3. Global-scale carbon and Alk budgets for all NEMO-PISCES sensitivity simulations. (*continued*)

https://doi.org/10.5194/egusphere-2025-523
Preprint. Discussion started: 13 February 2025
© Author(s) 2025. CC BY 4.0 License.

Figure B3. (*continued*). Carbon and Alk budgets (a) in absolute values for the standard simulation (std) and the simulation without riverine and burial fluxes of carbon and Alk (norivbur), or (b) relative to std for the other NEMO-PISCES sensitivity simulations. The type of representation is close to the one shared in Fig. 4c, but integrated over the whole ocean. All fluxes, in petagrams of carbon per year (PgC yr^{-1}) for carbon (in bold) and Alk (in normal font), are directed by arrows, with orientation indicating the sign, and size reflecting the absolute magnitude of the flux. In (b), only the fluxes (riverine discharge, as well as OM and $CaCO_3$ burial) with a significant anomaly are displayed, along with their associated changes relative to the standard simulation (std) in brackets, for both carbon (bold) and Alk (normal font). Additionally, values for carbon and Alk disequilibria (for simulations with a '-diseq' suffix), net addition flux (for atlpac, atlpac-diseq, and tropics-diseq), or the term of Alk restoration (for nosed-resto) is/are also shown when applicable (Table A1). In (a), for the standard simulation (std), a first approximation of the impact of OM and $CaCO_3$ production in the surface waters is also inferred from POC and PIC export at 100 m (in brackets with a star). Finally, in addition to the air-sea carbon flux (dark blue), the air-sea carbon flux stemming from global imbalance (light blue; Sect. 2.1.2 and Appendix B1.3 for an explanation of the residual imbalance) is also shared, as well as the associated inter-hemispheric air-sea carbon flux gradient (dark and light cyan). In (b), as the values are shown relative to the standard simulation (std), the simulated air-sea carbon flux anomalies are equivalent to the ones of the riverine/burial-driven air-sea carbon flux. A detailed description of the NEMO-PISCES sensitivity simulations can be found in Supplementary S1 and S2.

https://doi.org/10.5194/egusphere-2025-523
Preprint. Discussion started: 13 February 2025
© Author(s) 2025. CC BY 4.0 License.

Table B2. Literature review of the net air-sea carbon flux and its characterization. Bold lines are those accounting for external fluxes and boundaries at 20°S/N for the spatial distribution.

Source	Description of the method and further characterization		Net air-sea carbon flux					Inter-hemispheric transport of carbon
			South (<20°S)	Inter-tropics (20°S - 20°N)	North (>20°N)	Total	Inter-hemispheric gradient (north - south)	
		Moddeling approach[a]						
Murnane et al. (1999)	No external fluxes of carbon and Alk. The $CaCO_3$ reaching the seafloor is redissolved at the surface to conserve the global Alk inventory.	Princeton model	0.60[b]	-1.20[b]	0.60[b]	0.00	0.00[b]	
Sarmiento et al. (2000)	Intercomparison study of three ocean biogeochemistry models with the same implicit riverine discharge of 0.64 PgC yr^{-1} split between the northern and southern hemispheres (respectively -0.21 and -0.43 PgC yr^{-1} for the associated outgassing).	Princeton model	-0.55[c]		-0.09[c]	-0.64		
		IPSL model	-0.53[c]		-0.11[c]	-0.64		
		MPI model	-0.39[c]		-0.25[c]	-0.64		
Aumont et al. (2001)	No external fluxes of carbon and Alk. The $CaCO_3$ reaching the seafloor is redissolved at depth to conserve the global Alk inventory.	IPSL model	0.73	-1.40	0.67	0.00	-0.06	-0.10
	Carbon and Alk riverine discharge of respectively 0.81 and 0.40 PgC yr^{-1}, the global Alk inventory being conserved through an equivalent $CaCO_3$ burial. Regarding the riverine carbon (0.41 PgC yr^{-1}), 1/3 is injected as DIC at the river mouth and the rest is injected as DOC with an oxidation time-scale of 100 yr.	**IPSL model**	**0.43**	**-1.55**	**0.51**	**-0.61**	**0.08**	**-0.25**
Lacroix et al. (2020)	No external fluxes of carbon and Alk. The $CaCO_3$ reaching the seafloor is redissolved homogeneously at the surface to conserve the global Alk inventory, same for organic mater. This results in an equivalent implicit riverine discharge of 0.314 PgC yr^{-1} for carbon and 0.208 PgC yr^{-1} for Alk.	MPI model				-0.05		
	Constrained riverine discharge (0.603 PgC yr^{-1} for carbon and 0.366 PgC yr^{-1} for Alk) based on a hierarchy of weathering and terrestrial organic matter export models, while identifying regional hotspots of the riverine exports. OM and $CaCO_3$ burial are considered and not constrained (respectively 0.582 and 0.188 PgC yr^{-1}) , making free the global Alk inventory.	MPI model				0.18		
Present study (composite simulated estimate)	**Linear combination of sensitivity simulations to match literature estimates of the external sources/sinks of carbon and Alk**	**IPSL model**	**0.01 ± 0.13**	**-0.99 ± 0.10**	**0.51 ± 0.08**	**-0.46 ± 0.24**	**0.50 ± 0.15**	**-0.16 ± 0.08**

[a] All the ocean biogeochemistry model used in the following studies both account for the physical carbon pump and the biological one (soft-tissue and carbonate). [b] Boundaries at 15°S/N. [c] Boundaries at the equator.

(*continued*)

https://doi.org/10.5194/egusphere-2025-523
Preprint. Discussion started: 13 February 2025
© Author(s) 2025. CC BY 4.0 License.

(*continued*)

Source	Description of the method and further characterization		Net air-sea carbon flux South (<20°S)	Inter-tropics (20°S - 20°N)	North (>20°N)	Total	Inter-hemispheric gradient (north - south)	Inter-hemispheric transport of carbon
		Combined atmosphere-ocean inversion						
Sarmiento and Sundquist (1992)	Use of an ocean general circulation model (Sarmiento et al., 1992) to substract the simulated anthropogenic carbon uptake to the revised carbon budget by Tans et al. (1990) from a combination of an atmospheric transport model with a compilation of observations of air-sea CO_2 difference.		0.82[b]	-1.70[b]	0.28[b]	-0.60	0.54[b]	
Jacobson et al. (2007)	Use of a combination of transport inversions of atmospheric (constraining fluxes into the atmosphere from both land and ocean) and oceanic observations (constraining only air-sea fluxes), using multiple circulation models to assess the effects of errors in simulated transport. The ocean inversion estimates are corrected to remove the riverine carbon discharge (0.45 PgC yr^{-1}).					-0.39 ± 0.19		
		Ocean inversion						
Gloor et al. (2003)[e]	Use of an ocean general circulation model as well as observations of DIC and other tracers. The values were corrected to remove the riverine carbon discharge with the estimate (0.45 PgC yr^{-1}) from Jacobson et al. (2007).		0,32[d]	-1.35[d]	0.63[d]	-0.69	0.60[d]	
Mikaloff Fletcher et al. (2007)[f]	**Use of ten different ocean general circulation models (to quantify the error arising from uncertainties in the modeled transport) as well as observations of DIC and other tracers. The values were corrected to remove the riverine carbon discharge with the estimate (0.45 PgC yr^{-1}) from Jacobson et al. (2007).**		**0.21 ± 0.16**	**-1.10 ± 0.16**	**0.40 ± 0.14**	**-0.49 ± 0.27**	**0.19 ± 0.21**	**-0.19 ± 0.09**
		pCO_2-based						
Resplandy et al. (2018)	Reconstruction of the modern-day air-sea carbon flux from the global surface ocean pCO_2 field. The anthropogenic carbon flux is then extracted using an observationnally based reconstruction with a Green's function estimated from tracer data (Khatiwala et al., 2009) . The values were corrected to remove the riverine carbon discharge with the estimate (0.45 PgC yr^{-1}) from Jacobson et al. (2007).	Takahashi et al. (2009)	-0.16 ± 0.38	-1.09 ± 0.22	0.41 ± 0.23	-0.84 ± 0.50	0.57 ± 0.44	
		Wanninkhof et al. (2013)				-1.00 ± 0.67		
		Landschützer et al. (2014)	-0.04 ± 0.38	-1.11 ± 0.22	0.45 ± 0.23	-0.70 ± 0.50	0.49 ± 0.44	
	Same as above, except that riverine carbone discharge is constrained to ensure the closing of the ocean carbon budget (only considering air-sea fluxes and riverine carbon discharge).	Rödenbeck et al. (2013)	0.00 ± 0.38	-1.29 ± 0.22	0.51 ± 0.22	-0.78 ± 0.50	0.51 ± 0.44	-0.43
Regnier et al. (2022)	Reconstruction of the modern-day air-sea carbon flux from the global surface ocean pCO_2 field (Landschützer et al., 2014). The anthropogenic carbon flux is then extracted using three different methods: global ocean biogeochemistry models, ocean circulation inverse model, and pCO_2-based flux mapping models – with a post-correction applied to the latter for the rivers (0.6 PgC yr^{-1}) – (DeVries et al., 2019). The values were corrected to remove the riverine carbon discharge with the estimate (0.45 PgC yr^{-1}) from Jacobson et al. (2007).		0.20	-1.47	0.61	-0.65 ± 0.30	0.41	
		Mean ± std[g]	**0.00 ± 0.22**	**-1.24 ± 0.13**	**0.46 ± 0.13**	**-0.74 ± 0.29**	**0.46 ± 0.25**	

[b] Boundaries at 15°S/N. [d] Boundaries at 13°S/N. [e] The values were extracted from the Supplementary Figure of Mikaloff Fletcher et al. (2007). [f] Values from Resplandy et al. (2018).
[g] Accounting for all the pCO_2-based estimates, except the one by Wanninkhof et al. (2013), which is incomplete.

https://doi.org/10.5194/egusphere-2025-523
Preprint. Discussion started: 13 February 2025
© Author(s) 2025. CC BY 4.0 License.

Table B3. Literature review of the riverine/burial-driven air-sea carbon flux estimates, sharing also values and a description of the riverine discharge, OM burial, and $CaCO_3$ burial. The values obtained from the composite simulated estimate are also shared in grey. Note that its riverine discharge, OM burial and $CaCO_3$ fluxes (see Table 3) differ from those considered in the GCB and derived from Regnier et al. (2022), as we also account for flux on continental shelves.

Source	Riverine discharge		OM burial		$CaCO_3$ burial		Air-sea carbon outgassing from riverine and burial fluxes of carbon and Alk	Partitioning (south; inter-tropics; north) with boundaries at 20°S/N	
	Comment	Flux ($PgC\ yr^{-1}$)	Comment	Flux ($PgC\ yr^{-1}$)	Comment	Flux ($PgC\ yr^{-1}$)	($PgC\ yr^{-1}$)	Comment	Flux ($PgC\ yr^{-1}$)
Present study (composite simulated estimate)	Linear combination of sensitivity simulations to match literature estimates	0.90 ± 0.26	Linear combination of sensitivity simulations to match literature estimates	-0.11 ± 0.05	Linear combination of sensitivity simulations to match literature estimates	-0.25 ± 0.05	0.51 ± 0.24	Partitioning shared with boundaries at 20°S/N	$(0.15 \pm 0.13; 0.20 \pm 0.10; 0.16 \pm 0.08)$
								Partitioning shared with boundaries at 30°S/N	$(0.13 \pm 0.13; 0.24 \pm 0.12; 0.13 \pm 0.07)$
Regnier et al. (2022)	Mass balance calculation through the land-to-ocean aquatic continuum loop	0.80 ± 0.30	From literature	-0.04 ± 0.02	From literature	-0.13 ± 0.02	0.65 ± 0.30[a]	Using Lacroix et al. (2020) partitioning; e.g. Friedlingstein et al. (2023, 2024)	(0.09; 0.42; 0.14)
								Using Aumont et al. (2001) partitioning; e.g. Friedlingstein et al. (2022b)	(0.32; 0.16; 0.17)
Friedlingstein et al. (2020, 2022a)	Mean of Murnane et al. (1999) and Jacobson et al. (2007)	0.74	Mean of Resplandy et al. (2018) and Jacobson et al. (2007)	-0.05	Mean of Resplandy et al. (2018) and Jacobson et al. (2007)	-0.08	0.61	Using Aumont et al. (2001) partitioning; e.g. Friedlingstein et al. (2020, 2022a)	(0.30; 0.15; 0.16)
Lacroix et al. (2020)	From a hydrological discharge model	0.60	From an ocean biogeochemistry model	-0.19	From an ocean biogeochemistry model	-0.58	0.23[b]	Partitioning at the equator between southern and northern hemispheres	(0,11; 0.12)
Resplandy et al. (2018)	Scaled-up river flux of Jacobson et al. (2007) from heat based constraint	0.78 ± 0.41					0.78 ± 0.41	Using IPSL GOBM partitioning; e.g. Le Quéré et al. (2018b) and Friedlingstein et al. (2019)	(0.38; 0.19; 0.20)
								Using Jacobson et al. (2007) partitionning; e.g. Resplandy et al. (2018)	$(0.03 \pm 0.02; 0.38 \pm 0.19; 0.36 \pm 0.17)$
Jacobson et al. (2007)[c]	From global erosion model	0.71	From literature	-0.10	From literature	-0.16	0.45 ± 0.18[d]	Partitioning shared in Resplandy et al. (2018)	$(0.02 \pm 0.01; 0.22 \pm 0.11; 0.21 \pm 0.10)$
Aumont et al. (2001)	From a global erosion model	0.81			From an ocean biogeochemistry model to maintain a global Alk inventory at equilibrium	-0.2	0.61		(0.30; 0.15; 0.16)

[a] Rounded at $0.05\ PgC\ yr^{-1}$ in their paper. [b] Imbalance due to the consideration of a disturbance in the biological pump (production minus burial: $+0.45\ PgC\ yr^{-1}$), and the consideration of a free global Alk inventory. [c] Assumption that carbon from riverine discharge is not transported and that part of it is buried in the same region as well. [d] e.g. Le Quéré et al. (2016, 2018a).

https://doi.org/10.5194/egusphere-2025-523
Preprint. Discussion started: 13 February 2025
© Author(s) 2025. CC BY 4.0 License.

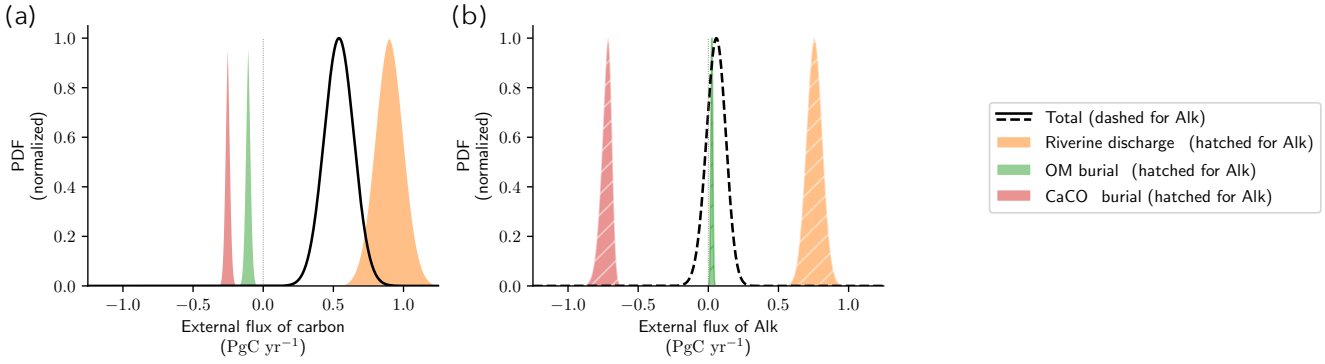

Figure B4. Literature-based estimates of the riverine discharge[a], OM burial[b] and $CaCO_3$ burial, with their associated uncertainties/extremes through normalized PDFs.

[a]Including groundwater discharge for both carbon and Alk, and anaerobic processes Alk.

[b]Including reverse weathering for Alk.

B3 Inter-hemispheric air-sea carbon flux gradient

We share additional insights regarding the inter-hemispheric air-sea carbon flux gradient, which is crucial for the global carbon cycle in its connection with the atmosphere and land (e.g. Keeling et al., 1989; Resplandy et al., 2018). It is thus valuable to distinguish in this inter-hemispheric gradient the component associated with the net air-sea carbon flux in both the southern and northern regions (Fig. B5).

Moreover, in order to underscore the importance of the carbon:Alk imbalance resulting from riverine and burial fluxes in shaping this inter-hemispheric air-sea carbon flux gradient, we decompose this gradient into two components accounting for regional imbalances: one associated with carbon and Alk from riverine and burial fluxes (including inventory disequilibria), and another originating from the inter-hemispheric transport of carbon and Alk (see Eq. 19 and Sect. 3.3.2; Fig. B6). The deviation from this partitioning in the NEMO-PISCES sensitivity simulations is small (less than 0.01 PgC yr^{-1}).

B4 Composite simulated estimate

We share (Fig. B7) the various components of the composite simulated estimate creation process as described in Sect. 2.3, and the results of which are presented in Sect. 3.3.3 (see Fig. 7 and Table B3).

https://doi.org/10.5194/egusphere-2025-523
Preprint. Discussion started: 13 February 2025
© Author(s) 2025. CC BY 4.0 License.

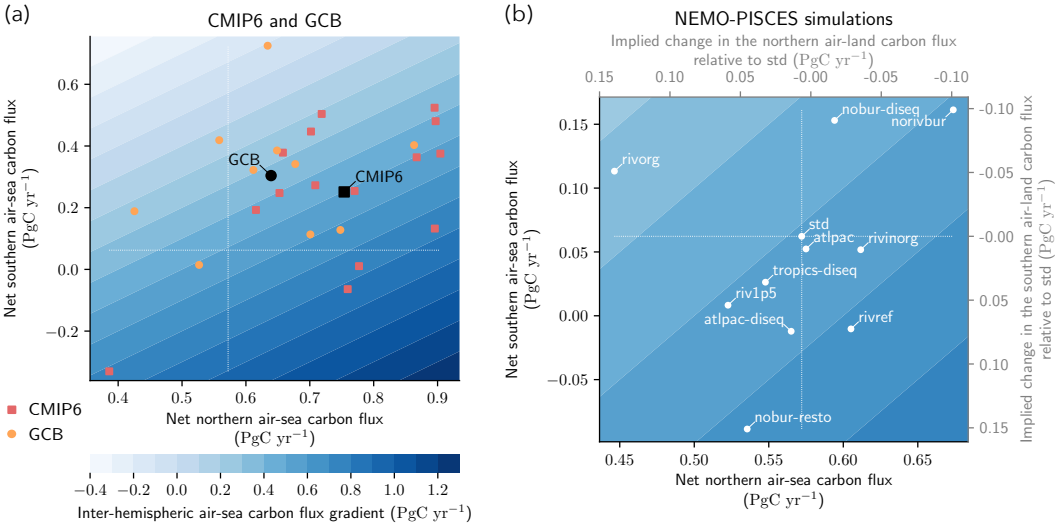

Figure B5. Decomposition of the inter-hemispheric air-sea carbon flux gradient (supplement to Fig. 2). Decomposition of the inter-hemispheric air-sea carbon flux gradient into the net southern and northen air-sea carbon fluxes for (a) CMIP6 and GCB, and (b) the NEMO-PISCES sensitivity simulations. Filled contours correspond to the inter-hemispheric air-sea carbon flux gradient. (a) The 15 CMIP6 ESMs (10 GCB GOBMs) are plotted with red squares (orange circles). The black square and circle refer to the CMIP6 and GCB ensemble means. In (b), secondary axes have been added to characterize the implied changes for the southern/northern air-land carbon flux relative to std, if the inter-hemispheric gradient is considered as well-represented. Then, a decrease in the net sourthern (northern) air-sea carbon flux relative to std entails an increase of the same magnitude in the net southern (northern) air-land carbon flux relative to std, and conversely.

640

https://doi.org/10.5194/egusphere-2025-523
Preprint. Discussion started: 13 February 2025
© Author(s) 2025. CC BY 4.0 License.

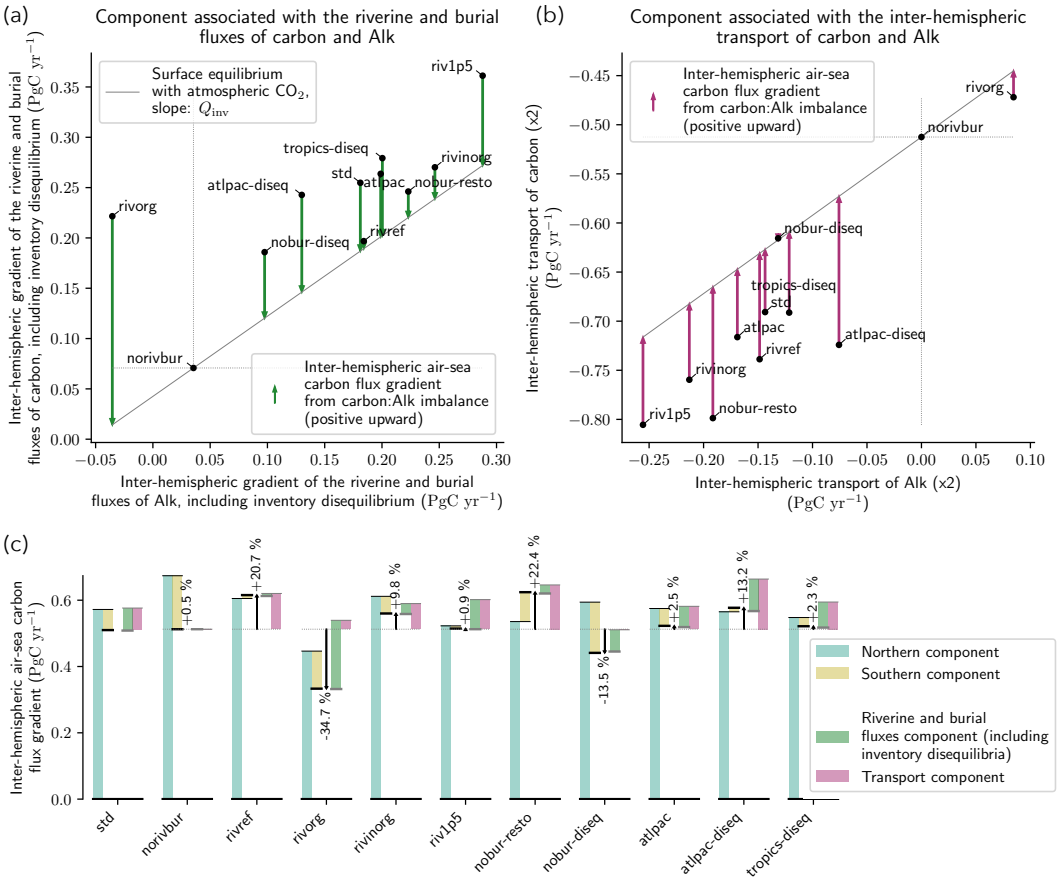

Figure B6. Partitioning of the inter-hemispheric air-sea carbon flux gradient from inter-hemispheric carbon:Alk imbalances (supplement to 6b). (a, b) Visual construction of the inter-hemispheric air-sea carbon flux gradient resulting from regional carbon:Alk imbalances due to (a) riverine and burial fluxes (including inventory disequilibria), and (b) inter-hemispheric transport, defining the values used in Fig. 6b. The reference was set on the simulation without riverine and burial fluxes (norivbur), so that the combination of the arrows of (a) and (b) results in the inter-hemispheric riverine/burial-driven air-sea carbon flux gradient. (c) Synthetic characterization for the whole set of NEMO-PISCES sensitivity simulations of the inter-hemispheric air-sea carbon flux gradient: with a southern/northern decomposition (as in Fig. B5b), and the partitioning resulting from regional carbon:Alk imbalances due to riverine and burial fluxes (including inventory disequilibria) – constructed in (a) –, and inter-hemispheric transport – constructed in (b).

https://doi.org/10.5194/egusphere-2025-523
Preprint. Discussion started: 13 February 2025
© Author(s) 2025. CC BY 4.0 License.

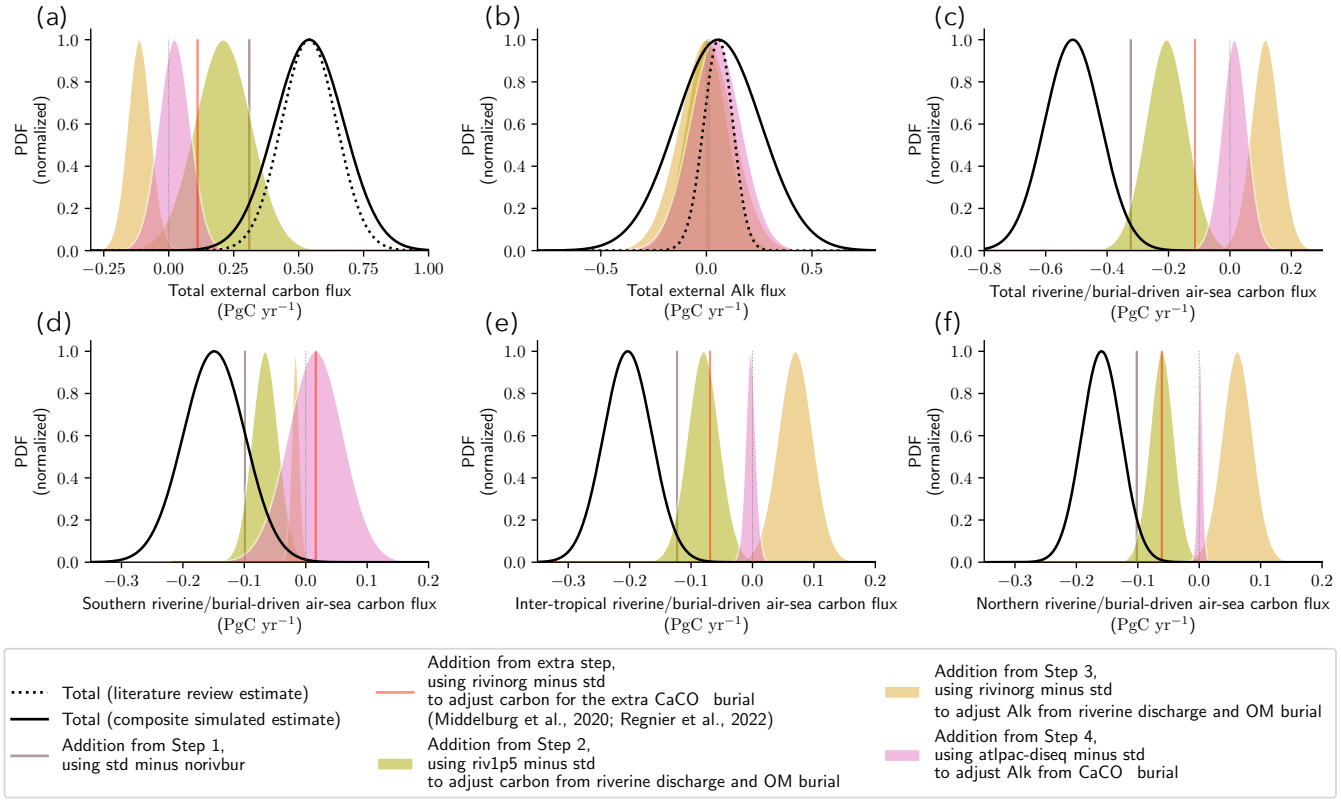

Figure B7. Components of the composite simulated estimate (supplement to Fig. 7). Each of the components represents the elements added at the different stages of the composite simulated estimate construction process (Steps 1, 2, 3, 4, and the extra step; Fig. A2). (a, b) Decomposition of the composite simulated estimate PDF associated with the total (a) carbon and (b) Alk external fluxes. (c, d, e, f) Characterization of the riverine/burial air-sea carbon flux in the composite simulated estimate, showing the various components for (c) the total value, as well as the (d) southern, (e) inter-tropical, and (f) northern regions. The black solid lines represent the total values for the composite simulated estimate, while the black dotted lines (a, b) correspond to the total carbon and Alk external fluxes from literature estimates (Fig. B4).

https://doi.org/10.5194/egusphere-2025-523
Preprint. Discussion started: 13 February 2025
© Author(s) 2025. CC BY 4.0 License.

Code availability. NEMO is released under the terms of the CeCILL licence. The standard NEMO-PISCES version (PISCESv2; Aumont et al., 2015) slightly modified in this study (see Sect. 2.2.1) is accessible through https://www.nemo-ocean.eu (last access: January 2025). The other NEMO-PISCES versions are available on request from the corresponding author.

Data availability. All the CMIP ensemble data were available on at least one of the Earth System Grid Federation (ESGF) nodes https://esgf-node.ipsl.upmc.fr/projects/esgf-ipsl/ (last access: January 2025). The 2024 release of GCB data is currently available via their SFTP server upon request but is expected to become directly accessible soon through their data browser platform https://mdosullivan.github.io/GCB/ (last access: January 2025). The code of all the various configurations of NEMO-PISCES used in this study is accessible on Zenodo (https://doi.org/10.5281/zenodo.8421951), as well as two supplementary figures, S1 and S2 (https://doi.org/10.5281/zenodo.8421898).

Author contributions. This work is in the framework of the OMIP-BGC group, which contributed collectively to this study through the organization and execution of the CMIP exercises and the sharing of simulation outputs. AP: conceptualization, investigation, methodology, formal analysis, visualization, writing – original draft preparation – and project administration. LB and LK: supervision, funding acquisition, methodology, resources, conceptualization, and writing – original draft preparation.

Competing interests. The contact author has declared that none of the authors has any competing interests.

Disclaimer. This article reflects only the authors' views; the funding agencies and their executive agencies are not responsible for any use that may be made of the information that the article contains.

Acknowledgements. Thanks to Olivier Aumont and Olivier Sulpis for the discussions we had, respectively, regarding the evolution of the riverine/burial-driven air-sea carbon flux assessment, and the burial of $CaCO_3$, as well as the global Alk inventory. We are grateful to the World Climate Research Programme's Working Group on Coupled Modelling, which is responsible for the CMIP exercises. For CMIP, the U.S. Department of Energy's Program for Climate Model Diagnosis and Intercomparison provided coordinating support and led the development of software infrastructure in partnership with the Global Organization for Earth System Science Portals. This study benefited from the ESPRI (Ensemble de Services Pour la Recherche à l'IPSL) computing and data centre (https://mesocentre.ipsl.fr, last access: January 2025), which is supported by CNRS, Sorbonne Université, École Polytechnique, and CNES and through national and international grants. We are grateful to the GCP for leading such a community effort around the carbon cycle, especially with yearly inter-model comparison exercises. We thank the PISCES community for actively using, developing, sharing knowledge around the marine biogeochemical model NEMO-PISCES (https://www.pisces-community.org, last access: January 2025). I would like to express my appreciation to the CEA (*Commissariat à l'Énergie Atomique et aux énergies alternatives*) and James C. Orr, the project coordinator of 'gen0040', for granting us access to the

https://doi.org/10.5194/egusphere-2025-523
Preprint. Discussion started: 13 February 2025
© Author(s) 2025. CC BY 4.0 License.

TGCC (*Très Grand Centre de Calcul*), particularly allowing us to conduct all our simulations on their 'Irène Rome' machine. Finally, we are also grateful to the administrative and technical staff at École Normale Supérieure/PSL.

Financial supports. Alban Planchat, Laurent Bopp and Lester Kwiatkowski are grateful to the ENS-Chanel research chair.

https://doi.org/10.5194/egusphere-2025-523
Preprint. Discussion started: 13 February 2025
© Author(s) 2025. CC BY 4.0 License.

References

Aumont, O., Orr, J. C., Monfray, P., Ludwig, W., Amiotte-Suchet, P., and Probst, J.-L.: Riverine-driven interhemispheric transport of carbon, Global Biogeochemical Cycles, 15, 393–405, https://doi.org/10.1029/1999GB001238, _eprint: https://onlinelibrary.wiley.com/doi/pdf/10.1029/1999GB001238, 2001.

Aumont, O., Ethé, C., Tagliabue, A., Bopp, L., and Gehlen, M.: PISCES-v2: an ocean biogeochemical model for carbon and ecosystem studies, Geoscientific Model Development, 8, 2465–2513, https://doi.org/10.5194/gmd-8-2465-2015, 2015.

Bopp, L., Aumont, O., Kwiatkowski, L., Clerc, C., Dupont, L., Ethé, C., Gorgues, T., Séférian, R., and Tagliabue, A.: Diazotrophy as a key driver of the response of marine net primary productivity to climate change, Biogeosciences, 19, 4267–4285, https://doi.org/10.5194/bg-19-4267-2022, 2022.

Boucher, O., Servonnat, J., Albright, A. L., Aumont, O., Balkanski, Y., Bastrikov, V., Bekki, S., Bonnet, R., Bony, S., Bopp, L., Braconnot, P., Brockmann, P., Cadule, P., Caubel, A., Cheruy, F., Codron, F., Cozic, A., Cugnet, D., D'Andrea, F., Davini, P., Lavergne, C., Denvil, S., Deshayes, J., Devilliers, M., Ducharne, A., Dufresne, J., Dupont, E., Éthé, C., Fairhead, L., Falletti, L., Flavoni, S., Foujols, M., Gardoll, S., Gastineau, G., Ghattas, J., Grandpeix, J., Guenet, B., Guez, E., L., Guilyardi, E., Guimberteau, M., Hauglustaine, D., Hourdin, F., Idelkadi, A., Joussaume, S., Kageyama, M., Khodri, M., Krinner, G., Lebas, N., Levavasseur, G., Lévy, C., Li, L., Lott, F., Lurton, T., Luyssaert, S., Madec, G., Madeleine, J., Maignan, F., Marchand, M., Marti, O., Mellul, L., Meurdesoif, Y., Mignot, J., Musat, I., Ottlé, C., Peylin, P., Planton, Y., Polcher, J., Rio, C., Rochetin, N., Rousset, C., Sepulchre, P., Sima, A., Swingedouw, D., Thiéblemont, R., Traore, A. K., Vancoppenolle, M., Vial, J., Vialard, J., Viovy, N., and Vuichard, N.: Presentation and Evaluation of the IPSL-CM6A-LR Climate Model, Journal of Advances in Modeling Earth Systems, 12, https://doi.org/10.1029/2019MS002010, 2020.

Boudreau, B. P., Middelburg, J. J., and Luo, Y.: The role of calcification in carbonate compensation, Nature Geoscience, 11, 894–900, https://doi.org/10.1038/s41561-018-0259-5, 2018.

Canadell, J., Monteiro, P., Costa, M., Cotrim da Cunha, L., Cox, P., Eliseev, A., Henson, S., Ishii, M., Jaccard, S., Koven, C., Lohila, A., Patra, P., Piao, S., Rogelj, J., Syampungani, S., Zaehle, S., and Zickfeld, K.: Global Carbon and other Biogeochemical Cycles and Feedbacks, in: Climate Change 2021: The Physical Science Basis. Contribution of Working Group I to the Sixth Assessment Report of the Intergovernmental Panel on Climate Change, edited by Masson-Delmotte, V., Zhai, P., Pirani, A., Connors, S., Péan, C., Berger, S., Caud, N., Chen, Y., Goldfarb, L., Gomis, M., Huang, M., Leitzell, K., Lonnoy, E., Matthews, J., Maycock, T., Waterfield, T., Yelekçi, O., Yu, R., and Zhou, B., pp. 673–816, Cambridge University Press, Cambridge, United Kingdom and New York, NY, USA, https://doi.org/10.1017/9781009157896.007, type: Book Section, 2021.

Cartapanis, O., Galbraith, E. D., Bianchi, D., and Jaccard, S. L.: Carbon burial in deep-sea sediment and implications for oceanic inventories of carbon and alkalinity over the last glacial cycle, Climate of the Past, 14, 1819–1850, https://doi.org/10.5194/cp-14-1819-2018, publisher: Copernicus GmbH, 2018.

Crisp, D., Dolman, H., Tanhua, T., McKinley, G. A., Hauck, J., Bastos, A., Sitch, S., Eggleston, S., and Aich, V.: How Well Do We Understand the Land-Ocean-Atmosphere Carbon Cycle?, Reviews of Geophysics, 60, e2021RG000 736, https://doi.org/10.1029/2021RG000736, publisher: John Wiley & Sons, Ltd, 2022.

DeVries, T., Le Quéré, C., Andrews, O., Berthet, S., Hauck, J., Ilyina, T., Landschützer, P., Lenton, A., Lima, I. D., Nowicki, M., Schwinger, J., and Séférian, R.: Decadal trends in the ocean carbon sink, Proceedings of the National Academy of Sciences, 116, 11 646–11 651, https://doi.org/10.1073/pnas.1900371116, publisher: Proceedings of the National Academy of Sciences, 2019.

https://doi.org/10.5194/egusphere-2025-523
Preprint. Discussion started: 13 February 2025
© Author(s) 2025. CC BY 4.0 License.

Dufresne, J.-L., Foujols, M.-A., Denvil, S., Caubel, A., Marti, O., Aumont, O., Balkanski, Y., Bekki, S., Bellenger, H., Benshila, R., Bony, S., Bopp, L., Braconnot, P., Brockmann, P., Cadule, P., Cheruy, F., Codron, F., Cozic, A., Cugnet, D., de Noblet, N., Duvel, J.-P., Ethé, C., Fairhead, L., Fichefet, T., Flavoni, S., Friedlingstein, P., Grandpeix, J.-Y., Guez, L., Guilyardi, E., Hauglustaine, D., Hourdin, F., Idelkadi, A., Ghattas, J., Joussaume, S., Kageyama, M., Krinner, G., Labetoulle, S., Lahellec, A., Lefebvre, M.-P., Lefevre, F., Levy, C., Li, Z. X., Lloyd, J., Lott, F., Madec, G., Mancip, M., Marchand, M., Masson, S., Meurdesoif, Y., Mignot, J., Musat, I., Parouty, S., Polcher, J., Rio, C., Schulz, M., Swingedouw, D., Szopa, S., Talandier, C., Terray, P., Viovy, N., and Vuichard, N.: Climate change projections using the IPSL-CM5 Earth System Model: from CMIP3 to CMIP5, Climate Dynamics, 40, 2123–2165, https://doi.org/10.1007/s00382-012-1636-1, 2013.

Eyring, V., Bony, S., Meehl, G. A., Senior, C. A., Stevens, B., Stouffer, R. J., and Taylor, K. E.: Overview of the Coupled Model Intercomparison Project Phase 6 (CMIP6) experimental design and organization, Geoscientific Model Development, 9, 1937–1958, https://doi.org/10.5194/gmd-9-1937-2016, 2016.

Friedlingstein, P., Jones, M. W., O'Sullivan, M., Andrew, R. M., Hauck, J., Peters, G. P., Peters, W., Pongratz, J., Sitch, S., Le Quéré, C., Bakker, D. C. E., Canadell, J. G., Ciais, P., Jackson, R. B., Anthoni, P., Barbero, L., Bastos, A., Bastrikov, V., Becker, M., Bopp, L., Buitenhuis, E., Chandra, N., Chevallier, F., Chini, L. P., Currie, K. I., Feely, R. A., Gehlen, M., Gilfillan, D., Gkritzalis, T., Goll, D. S., Gruber, N., Gutekunst, S., Harris, I., Haverd, V., Houghton, R. A., Hurtt, G., Ilyina, T., Jain, A. K., Joetzjer, E., Kaplan, J. O., Kato, E., Klein Goldewijk, K., Korsbakken, J. I., Landschützer, P., Lauvset, S. K., Lefèvre, N., Lenton, A., Lienert, S., Lombardozzi, D., Marland, G., McGuire, P. C., Melton, J. R., Metzl, N., Munro, D. R., Nabel, J. E. M. S., Nakaoka, S.-I., Neill, C., Omar, A. M., Ono, T., Peregon, A., Pierrot, D., Poulter, B., Rehder, G., Resplandy, L., Robertson, E., Rödenbeck, C., Séférian, R., Schwinger, J., Smith, N., Tans, P. P., Tian, H., Tilbrook, B., Tubiello, F. N., van der Werf, G. R., Wiltshire, A. J., and Zaehle, S.: Global Carbon Budget 2019, Earth System Science Data, 11, 1783–1838, https://doi.org/10.5194/essd-11-1783-2019, publisher: Copernicus GmbH, 2019.

Friedlingstein, P., O'Sullivan, M., Jones, M. W., Andrew, R. M., Hauck, J., Olsen, A., Peters, G. P., Peters, W., Pongratz, J., Sitch, S., Le Quéré, C., Canadell, J. G., Ciais, P., Jackson, R. B., Alin, S., Aragão, L. E. O. C., Arneth, A., Arora, V., Bates, N. R., Becker, M., Benoit-Cattin, A., Bittig, H. C., Bopp, L., Bultan, S., Chandra, N., Chevallier, F., Chini, L. P., Evans, W., Florentie, L., Forster, P. M., Gasser, T., Gehlen, M., Gilfillan, D., Gkritzalis, T., Gregor, L., Gruber, N., Harris, I., Hartung, K., Haverd, V., Houghton, R. A., Ilyina, T., Jain, A. K., Joetzjer, E., Kadono, K., Kato, E., Kitidis, V., Korsbakken, J. I., Landschützer, P., Lefèvre, N., Lenton, A., Lienert, S., Liu, Z., Lombardozzi, D., Marland, G., Metzl, N., Munro, D. R., Nabel, J. E. M. S., Nakaoka, S.-I., Niwa, Y., O'Brien, K., Ono, T., Palmer, P. I., Pierrot, D., Poulter, B., Resplandy, L., Robertson, E., Rödenbeck, C., Schwinger, J., Séférian, R., Skjelvan, I., Smith, A. J. P., Sutton, A. J., Tanhua, T., Tans, P. P., Tian, H., Tilbrook, B., van der Werf, G., Vuichard, N., Walker, A. P., Wanninkhof, R., Watson, A. J., Willis, D., Wiltshire, A. J., Yuan, W., Yue, X., and Zaehle, S.: Global Carbon Budget 2020, Earth System Science Data, 12, 3269–3340, https://doi.org/10.5194/essd-12-3269-2020, publisher: Copernicus GmbH, 2020.

Friedlingstein, P., Jones, M. W., O'Sullivan, M., Andrew, R. M., Bakker, D. C. E., Hauck, J., Le Quéré, C., Peters, G. P., Peters, W., Pongratz, J., Sitch, S., Canadell, J. G., Ciais, P., Jackson, R. B., Alin, S. R., Anthoni, P., Bates, N. R., Becker, M., Bellouin, N., Bopp, L., Chau, T. T. T., Chevallier, F., Chini, L. P., Cronin, M., Currie, K. I., Decharme, B., Djeutchouang, L. M., Dou, X., Evans, W., Feely, R. A., Feng, L., Gasser, T., Gilfillan, D., Gkritzalis, T., Grassi, G., Gregor, L., Gruber, N., Gürses, , Harris, I., Houghton, R. A., Hurtt, G. C., Iida, Y., Ilyina, T., Luijkx, I. T., Jain, A., Jones, S. D., Kato, E., Kennedy, D., Klein Goldewijk, K., Knauer, J., Korsbakken, J. I., Körtzinger, A., Landschützer, P., Lauvset, S. K., Lefèvre, N., Lienert, S., Liu, J., Marland, G., McGuire, P. C., Melton, J. R., Munro, D. R., Nabel, J. E. M. S., Nakaoka, S.-I., Niwa, Y., Ono, T., Pierrot, D., Poulter, B., Rehder, G., Resplandy, L., Robertson, E., Rödenbeck, C., Rosan, T. M., Schwinger, J., Schwingshackl, C., Séférian, R., Sutton, A. J., Sweeney, C., Tanhua, T., Tans, P. P., Tian, H., Tilbrook, B., Tubiello,

https://doi.org/10.5194/egusphere-2025-523
Preprint. Discussion started: 13 February 2025
© Author(s) 2025. CC BY 4.0 License.

F., van der Werf, G. R., Vuichard, N., Wada, C., Wanninkhof, R., Watson, A. J., Willis, D., Wiltshire, A. J., Yuan, W., Yue, C., Yue, X., Zaehle, S., and Zeng, J.: Global Carbon Budget 2021, Earth System Science Data, 14, 1917–2005, https://doi.org/10.5194/essd-14-1917-2022, publisher: Copernicus GmbH, 2022a.

Friedlingstein, P., O'Sullivan, M., Jones, M. W., Andrew, R. M., Gregor, L., Hauck, J., Le Quéré, C., Luijkx, I. T., Olsen, A., Peters, G. P., Peters, W., Pongratz, J., Schwingshackl, C., Sitch, S., Canadell, J. G., Ciais, P., Jackson, R. B., Alin, S. R., Alkama, R., Arneth, A., Arora, V. K., Bates, N. R., Becker, M., Bellouin, N., Bittig, H. C., Bopp, L., Chevallier, F., Chini, L. P., Cronin, M., Evans, W., Falk, S., Feely, R. A., Gasser, T., Gehlen, M., Gkritzalis, T., Gloege, L., Grassi, G., Gruber, N., Gürses, , Harris, I., Hefner, M., Houghton, R. A., Hurtt, G. C., Iida, Y., Ilyina, T., Jain, A. K., Jersild, A., Kadono, K., Kato, E., Kennedy, D., Klein Goldewijk, K., Knauer, J., Korsbakken, J. I., Landschützer, P., Lefèvre, N., Lindsay, K., Liu, J., Liu, Z., Marland, G., Mayot, N., McGrath, M. J., Metzl, N., Monacci, N. M., Munro, D. R., Nakaoka, S.-I., Niwa, Y., O'Brien, K., Ono, T., Palmer, P. I., Pan, N., Pierrot, D., Pocock, K., Poulter, B., Resplandy, L., Robertson, E., Rödenbeck, C., Rodriguez, C., Rosan, T. M., Schwinger, J., Séférian, R., Shutler, J. D., Skjelvan, I., Steinhoff, T., Sun, Q., Sutton, A. J., Sweeney, C., Takao, S., Tanhua, T., Tans, P. P., Tian, X., Tian, H., Tilbrook, B., Tsujino, H., Tubiello, F., van der Werf, G. R., Walker, A. P., Wanninkhof, R., Whitehead, C., Willstrand Wranne, A., Wright, R., Yuan, W., Yue, C., Yue, X., Zaehle, S., Zeng, J., and Zheng, B.: Global Carbon Budget 2022, Earth System Science Data, 14, 4811–4900, https://doi.org/10.5194/essd-14-4811-2022, publisher: Copernicus GmbH, 2022b.

Friedlingstein, P., O'Sullivan, M., Jones, M. W., Andrew, R. M., Bakker, D. C. E., Hauck, J., Landschützer, P., Le Quéré, C., Luijkx, I. T., Peters, G. P., Peters, W., Pongratz, J., Schwingshackl, C., Sitch, S., Canadell, J. G., Ciais, P., Jackson, R. B., Alin, S. R., Anthoni, P., Barbero, L., Bates, N. R., Becker, M., Bellouin, N., Decharme, B., Bopp, L., Brasika, I. B. M., Cadule, P., Chamberlain, M. A., Chandra, N., Chau, T.-T.-T., Chevallier, F., Chini, L. P., Cronin, M., Dou, X., Enyo, K., Evans, W., Falk, S., Feely, R. A., Feng, L., Ford, D. J., Gasser, T., Ghattas, J., Gkritzalis, T., Grassi, G., Gregor, L., Gruber, N., Gürses, , Harris, I., Hefner, M., Heinke, J., Houghton, R. A., Hurtt, G. C., Iida, Y., Ilyina, T., Jacobson, A. R., Jain, A., Jarníková, T., Jersild, A., Jiang, F., Jin, Z., Joos, F., Kato, E., Keeling, R. F., Kennedy, D., Klein Goldewijk, K., Knauer, J., Korsbakken, J. I., Körtzinger, A., Lan, X., Lefèvre, N., Li, H., Liu, J., Liu, Z., Ma, L., Marland, G., Mayot, N., McGuire, P. C., McKinley, G. A., Meyer, G., Morgan, E. J., Munro, D. R., Nakaoka, S.-I., Niwa, Y., O'Brien, K. M., Olsen, A., Omar, A. M., Ono, T., Paulsen, M., Pierrot, D., Pocock, K., Poulter, B., Powis, C. M., Rehder, G., Resplandy, L., Robertson, E., Rödenbeck, C., Rosan, T. M., Schwinger, J., Séférian, R., Smallman, T. L., Smith, S. M., Sospedra-Alfonso, R., Sun, Q., Sutton, A. J., Sweeney, C., Takao, S., Tans, P. P., Tian, H., Tilbrook, B., Tsujino, H., Tubiello, F., van der Werf, G. R., van Ooijen, E., Wanninkhof, R., Watanabe, M., Wimart-Rousseau, C., Yang, D., Yang, X., Yuan, W., Yue, X., Zaehle, S., Zeng, J., and Zheng, B.: Global Carbon Budget 2023, Earth System Science Data, 15, 5301–5369, https://doi.org/10.5194/essd-15-5301-2023, publisher: Copernicus GmbH, 2023.

Friedlingstein, P., O'Sullivan, M., Jones, M. W., Andrew, R. M., Hauck, J., Landschützer, P., Le Quéré, C., Li, H., Luijkx, I. T., Olsen, A., Peters, G. P., Peters, W., Pongratz, J., Schwingshackl, C., Sitch, S., Canadell, J. G., Ciais, P., Jackson, R. B., Alin, S. R., Arneth, A., Arora, V., Bates, N. R., Becker, M., Bellouin, N., Berghoff, C. F., Bittig, H. C., Bopp, L., Cadule, P., Campbell, K., Chamberlain, M. A., Chandra, N., Chevallier, F., Chini, L. P., Colligan, T., Decayeux, J., Djeutchouang, L., Dou, X., Duran Rojas, C., Enyo, K., Evans, W., Fay, A., Feely, R. A., Ford, D. J., Foster, A., Gasser, T., Gehlen, M., Gkritzalis, T., Grassi, G., Gregor, L., Gruber, N., Gürses, , Harris, I., Hefner, M., Heinke, J., Hurtt, G. C., Iida, Y., Ilyina, T., Jacobson, A. R., Jain, A., Jarníková, T., Jersild, A., Jiang, F., Jin, Z., Kato, E., Keeling, R. F., Klein Goldewijk, K., Knauer, J., Korsbakken, J. I., Lauvset, S. K., Lefèvre, N., Liu, Z., Liu, J., Ma, L., Maksyutov, S., Marland, G., Mayot, N., McGuire, P., Metzl, N., Monacci, N. M., Morgan, E. J., Nakaoka, S.-I., Neill, C., Niwa, Y., Nützel, T., Olivier, L., Ono, T., Palmer, P. I., Pierrot, D., Qin, Z., Resplandy, L., Roobaert, A., Rosan, T. M., Rödenbeck, C., Schwinger, J., Smallman, T. L., Smith, S., Sospedra-Alfonso, R., Steinhoff, T., Sun, Q., Sutton, A. J., Séférian, R., Takao, S., Tatebe, H., Tian, H., Tilbrook, B., Torres, O., Tourigny,

https://doi.org/10.5194/egusphere-2025-523
Preprint. Discussion started: 13 February 2025
© Author(s) 2025. CC BY 4.0 License.

E., Tsujino, H., Tubiello, F., van der Werf, G., Wanninkhof, R., Wang, X., Yang, D., Yang, X., Yu, Z., Yuan, W., Yue, X., Zaehle, S., Zeng, N., and Zeng, J.: Global Carbon Budget 2024, https://doi.org/10.5194/essd-2024-519, publisher: Copernicus GmbH, 2024.

Gloor, M., Gruber, N., Sarmiento, J., Sabine, C. L., Feely, R. A., and Rödenbeck, C.: A first estimate of present and preindustrial air-sea CO2 flux patterns based on ocean interior carbon measurements and models, Geophysical Research Letters, 30, 10–1–10–4, https://doi.org/10.1029/2002GL015594, _eprint: https://onlinelibrary.wiley.com/doi/pdf/10.1029/2002GL015594, 2003.

Gruber, N., Gloor, M., Mikaloff Fletcher, S. E., Doney, S. C., Dutkiewicz, S., Follows, M. J., Gerber, M., Jacobson, A. R., Joos, F., Lindsay, K., Menemenlis, D., Mouchet, A., Müller, S. A., Sarmiento, J. L., and Takahashi, T.: Oceanic sources, sinks, and transport of atmospheric CO2, Global Biogeochemical Cycles, 23, https://doi.org/10.1029/2008GB003349, _eprint: https://onlinelibrary.wiley.com/doi/pdf/10.1029/2008GB003349, 2009.

Gruber, N., Bakker, D. C. E., DeVries, T., Gregor, L., Hauck, J., Landschützer, P., McKinley, G. A., and Müller, J. D.: Trends and variability in the ocean carbon sink, Nature Reviews Earth & Environment, 4, 119–134, https://doi.org/10.1038/s43017-022-00381-x, 2023.

Hauck, J., Zeising, M., Le Quéré, C., Gruber, N., Bakker, D. C. E., Bopp, L., Chau, T. T. T., Gürses, , Ilyina, T., Landschützer, P., Lenton, A., Resplandy, L., Rödenbeck, C., Schwinger, J., and Séférian, R.: Consistency and Challenges in the Ocean Carbon Sink Estimate for the Global Carbon Budget, Frontiers in Marine Science, 7, https://www.frontiersin.org/article/10.3389/fmars.2020.571720, 2020.

Hauck, J., Mayot, N., Gregor, L., Bopp, L., Gehlen, M., Gloege, L., Gruber, N., Gürses, , Iida, Y., Ilyina, T., Jersild, A., Lindsay, K., Resplandy, L., Rödenbeck, C., Schwinger, J., Seferian, R., Shutler, J., Tsujino, H., Wright, R., and Zeng, J.: Global Carbon Budget 2022, surface ocean fugactiy of CO2 (fCO2) and air-sea CO2 flux of individual Global ocean biogechemical models and surface ocean fCO2-based data-products, https://doi.org/10.5281/zenodo.7273309, 2022.

Hauck, J., Nissen, C., Landschützer, P., Rödenbeck, C., Bushinsky, S., and Olsen, A.: Sparse observations induce large biases in estimates of the global ocean CO_2 sink: an ocean model subsampling experiment, Philosophical Transactions of the Royal Society A: Mathematical, Physical and Engineering Sciences, 381, 20220 063, https://doi.org/10.1098/rsta.2022.0063, 2023.

Humphreys, M. P., Daniels, C. J., Wolf-Gladrow, D. A., Tyrrell, T., and Achterberg, E. P.: On the influence of marine biogeochemical processes over CO2 exchange between the atmosphere and ocean, Marine Chemistry, 199, 1–11, https://doi.org/10.1016/j.marchem.2017.12.006, 2018.

Jacobson, A. R., Mikaloff Fletcher, S. E., Gruber, N., Sarmiento, J. L., and Gloor, M.: A joint atmosphere-ocean inversion for surface fluxes of carbon dioxide: 1. Methods and global-scale fluxes, Global Biogeochemical Cycles, 21, https://doi.org/10.1029/2005GB002556, _eprint: https://onlinelibrary.wiley.com/doi/pdf/10.1029/2005GB002556, 2007.

Keeling, C. D., Bacastow, R. B., Carter, A. F., Piper, S. C., Whorf, T. P., Heimann, M., Mook, W. G., and Roeloffzen, H.: A three-dimensional model of atmospheric CO2 transport based on observed winds: 1. Analysis of observational data, in: Aspects of Climate Variability in the Pacific and the Western Americas, pp. 165–236, American Geophysical Union (AGU), ISBN 978-1-118-66428-5, https://doi.org/10.1029/GM055p0165, _eprint: https://onlinelibrary.wiley.com/doi/pdf/10.1029/GM055p0165, 1989.

Khatiwala, S., Primeau, F., and Hall, T.: Reconstruction of the history of anthropogenic CO2 concentrations in the ocean, Nature, 462, 346–349, https://doi.org/10.1038/nature08526, 2009.

Lacroix, F., Ilyina, T., and Hartmann, J.: Oceanic CO_2 outgassing and biological production hotspots induced by pre-industrial river loads of nutrients and carbon in a global modeling approach, Biogeosciences, 17, 55–88, https://doi.org/10.5194/bg-17-55-2020, publisher: Copernicus GmbH, 2020.

https://doi.org/10.5194/egusphere-2025-523
Preprint. Discussion started: 13 February 2025
© Author(s) 2025. CC BY 4.0 License.

Landschützer, P., Gruber, N., Bakker, D. C. E., and Schuster, U.: Recent variability of the global ocean carbon sink, Global Biogeochemical Cycles, 28, 927–949, https://doi.org/10.1002/2014GB004853, _eprint: https://onlinelibrary.wiley.com/doi/pdf/10.1002/2014GB004853, 2014.

Le Quéré, C., Andrew, R. M., Canadell, J. G., Sitch, S., Korsbakken, J. I., Peters, G. P., Manning, A. C., Boden, T. A., Tans, P. P., Houghton, R. A., Keeling, R. F., Alin, S., Andrews, O. D., Anthoni, P., Barbero, L., Bopp, L., Chevallier, F., Chini, L. P., Ciais, P., Currie, K., Delire, C., Doney, S. C., Friedlingstein, P., Gkritzalis, T., Harris, I., Hauck, J., Haverd, V., Hoppema, M., Klein Goldewijk, K., Jain, A. K., Kato, E., Körtzinger, A., Landschützer, P., Lefèvre, N., Lenton, A., Lienert, S., Lombardozzi, D., Melton, J. R., Metzl, N., Millero, F., Monteiro, P. M. S., Munro, D. R., Nabel, J. E. M. S., Nakaoka, S.-i., O'Brien, K., Olsen, A., Omar, A. M., Ono, T., Pierrot, D., Poulter, B., Rödenbeck, C., Salisbury, J., Schuster, U., Schwinger, J., Séférian, R., Skjelvan, I., Stocker, B. D., Sutton, A. J., Takahashi, T., Tian, H., Tilbrook, B., van der Laan-Luijkx, I. T., van der Werf, G. R., Viovy, N., Walker, A. P., Wiltshire, A. J., and Zaehle, S.: Global Carbon Budget 2016, Earth System Science Data, 8, 605–649, https://doi.org/10.5194/essd-8-605-2016, publisher: Copernicus GmbH, 2016.

Le Quéré, C., Andrew, R. M., Friedlingstein, P., Sitch, S., Hauck, J., Pongratz, J., Pickers, P. A., Korsbakken, J. I., Peters, G. P., Canadell, J. G., Arneth, A., Arora, V. K., Barbero, L., Bastos, A., Bopp, L., Chevallier, F., Chini, L. P., Ciais, P., Doney, S. C., Gkritzalis, T., Goll, D. S., Harris, I., Haverd, V., Hoffman, F. M., Hoppema, M., Houghton, R. A., Hurtt, G., Ilyina, T., Jain, A. K., Johannessen, T., Jones, C. D., Kato, E., Keeling, R. F., Goldewijk, K. K., Landschützer, P., Lefèvre, N., Lienert, S., Liu, Z., Lombardozzi, D., Metzl, N., Munro, D. R., Nabel, J. E. M. S., Nakaoka, S.-i., Neill, C., Olsen, A., Ono, T., Patra, P., Peregon, A., Peters, W., Peylin, P., Pfeil, B., Pierrot, D., Poulter, B., Rehder, G., Resplandy, L., Robertson, E., Rocher, M., Rödenbeck, C., Schuster, U., Schwinger, J., Séférian, R., Skjelvan, I., Steinhoff, T., Sutton, A., Tans, P. P., Tian, H., Tilbrook, B., Tubiello, F. N., van der Laan-Luijkx, I. T., van der Werf, G. R., Viovy, N., Walker, A. P., Wiltshire, A. J., Wright, R., Zaehle, S., and Zheng, B.: Global Carbon Budget 2018, Earth System Science Data, 10, 2141–2194, https://doi.org/10.5194/essd-10-2141-2018, publisher: Copernicus GmbH, 2018a.

Le Quéré, C., Andrew, R. M., Friedlingstein, P., Sitch, S., Pongratz, J., Manning, A. C., Korsbakken, J. I., Peters, G. P., Canadell, J. G., Jackson, R. B., Boden, T. A., Tans, P. P., Andrews, O. D., Arora, V. K., Bakker, D. C. E., Barbero, L., Becker, M., Betts, R. A., Bopp, L., Chevallier, F., Chini, L. P., Ciais, P., Cosca, C. E., Cross, J., Currie, K., Gasser, T., Harris, I., Hauck, J., Haverd, V., Houghton, R. A., Hunt, C. W., Hurtt, G., Ilyina, T., Jain, A. K., Kato, E., Kautz, M., Keeling, R. F., Klein Goldewijk, K., Körtzinger, A., Landschützer, P., Lefèvre, N., Lenton, A., Lienert, S., Lima, I., Lombardozzi, D., Metzl, N., Millero, F., Monteiro, P. M. S., Munro, D. R., Nabel, J. E. M. S., Nakaoka, S.-i., Nojiri, Y., Padin, X. A., Peregon, A., Pfeil, B., Pierrot, D., Poulter, B., Rehder, G., Reimer, J., Rödenbeck, C., Schwinger, J., Séférian, R., Skjelvan, I., Stocker, B. D., Tian, H., Tilbrook, B., Tubiello, F. N., van der Laan-Luijkx, I. T., van der Werf, G. R., van Heuven, S., Viovy, N., Vuichard, N., Walker, A. P., Watson, A. J., Wiltshire, A. J., Zaehle, S., and Zhu, D.: Global Carbon Budget 2017, Earth System Science Data, 10, 405–448, https://doi.org/10.5194/essd-10-405-2018, publisher: Copernicus GmbH, 2018b.

Li, M., Peng, C., Wang, M., Xue, W., Zhang, K., Wang, K., Shi, G., and Zhu, Q.: The carbon flux of global rivers: A re-evaluation of amount and spatial patterns, Ecological Indicators, 80, 40–51, https://doi.org/10.1016/j.ecolind.2017.04.049, 2017.

Ludwig, W., Amiotte Suchet, P., and Probst, J.-L.: River discharges of carbon to the world's oceans: determining local inputs of alkalinity and of dissolved and particulate organic carbon, Sciences de la terre et des planètes (Comptes rendus de l'Académie des sciences), t. 323, 1007–1014, https://oatao.univ-toulouse.fr/3498/, publisher: Gauthier-Villars, 1996.

Middelburg, J. J., Soetaert, K., and Hagens, M.: Ocean Alkalinity, Buffering and Biogeochemical Processes, Reviews of Geophysics, 58, https://doi.org/10.1029/2019RG000681, 2020.

Mikaloff Fletcher, S. E., Gruber, N., Jacobson, A. R., Gloor, M., Doney, S. C., Dutkiewicz, S., Gerber, M., Follows, M., Joos, F., Lindsay, K., Menemenlis, D., Mouchet, A., Müller, S. A., and Sarmiento, J. L.: Inverse estimates of the oceanic sources and sinks of natu-

https://doi.org/10.5194/egusphere-2025-523
Preprint. Discussion started: 13 February 2025
© Author(s) 2025. CC BY 4.0 License.

ral CO2 and the implied oceanic carbon transport, Global Biogeochemical Cycles, 21, https://doi.org/10.1029/2006GB002751, _eprint: https://onlinelibrary.wiley.com/doi/pdf/10.1029/2006GB002751, 2007.

Milliman, J. D.: Production and accumulation of calcium carbonate in the ocean: Budget of a nonsteady state, Global Biogeochemical Cycles, 7, 927–957, https://doi.org/10.1029/93GB02524, 1993.

Murnane, R. J., Sarmiento, J. L., and Le Quéré, C.: Spatial distribution of air-sea CO2 fluxes and the interhemispheric transport of carbon by the oceans, Global Biogeochemical Cycles, 13, 287–305, https://doi.org/10.1029/1998GB900009, _eprint: https://onlinelibrary.wiley.com/doi/pdf/10.1029/1998GB900009, 1999.

Orr, J. C., Najjar, R. G., Aumont, O., Bopp, L., Bullister, J. L., Danabasoglu, G., Doney, S. C., Dunne, J. P., Dutay, J.-C., Graven, H., Griffies, S. M., John, J. G., Joos, F., Levin, I., Lindsay, K., Matear, R. J., McKinley, G. A., Mouchet, A., Oschlies, A., Romanou, A., Schlitzer, R., Tagliabue, A., Tanhua, T., and Yool, A.: Biogeochemical protocols and diagnostics for the CMIP6 Ocean Model Intercomparison Project (OMIP), Geoscientific Model Development, 10, 2169–2199, https://doi.org/10.5194/gmd-10-2169-2017, 2017.

Planchat, A., Kwiatkowski, L., Bopp, L., Torres, O., Christian, J. R., Butenschön, M., Lovato, T., Séférian, R., Chamberlain, M. A., Aumont, O., Watanabe, M., Yamamoto, A., Yool, A., Ilyina, T., Tsujino, H., Krumhardt, K. M., Schwinger, J., Tjiputra, J., Dunne, J. P., and Stock, C.: The representation of alkalinity and the carbonate pump from CMIP5 to CMIP6 Earth system models and implications for the carbon cycle, Biogeosciences, 20, 1195–1257, https://doi.org/10.5194/bg-20-1195-2023, publisher: Copernicus GmbH, 2023.

Regnier, P., Resplandy, L., Najjar, R. G., and Ciais, P.: The land-to-ocean loops of the global carbon cycle, Nature, 603, 401–410, https://doi.org/10.1038/s41586-021-04339-9, 2022.

Resplandy, L., Keeling, R. F., Rödenbeck, C., Stephens, B. B., Khatiwala, S., Rodgers, K. B., Long, M. C., Bopp, L., and Tans, P. P.: Revision of global carbon fluxes based on a reassessment of oceanic and riverine carbon transport, Nature Geoscience, 11, 504–509, https://doi.org/10.1038/s41561-018-0151-3, number: 7 Publisher: Nature Publishing Group, 2018.

Revelle, R. and Suess, H. E.: Carbon Dioxide Exchange Between Atmosphere and Ocean and the Question of an Increase of Atmospheric CO_2 during the Past Decades, Tellus, 9, 18–27, https://doi.org/10.1111/j.2153-3490.1957.tb01849.x, 1957.

Ridgwell, A. and Zeebe, R.: The role of the global carbonate cycle in the regulation and evolution of the Earth system, Earth and Planetary Science Letters, 234, 299–315, https://doi.org/10.1016/j.epsl.2005.03.006, 2005.

Rödenbeck, C., Keeling, R. F., Bakker, D. C. E., Metzl, N., Olsen, A., Sabine, C., and Heimann, M.: Global surface-ocean p^{CO_2} and sea–air CO_2 flux variability from an observation-driven ocean mixed-layer scheme, Ocean Science, 9, 193–216, https://doi.org/10.5194/os-9-193-2013, publisher: Copernicus GmbH, 2013.

Sarmiento, J. L. and Gruber, N.: Ocean biogeochemical dynamics, Princeton University Press, Princeton, ISBN 978-0-691-01707-5, oCLC: ocm60651167, 2006.

Sarmiento, J. L. and Sundquist, E. T.: Revised budget for the oceanic uptake of anthropogenic carbon dioxide, Nature, 356, 589–593, https://doi.org/10.1038/356589a0, 1992.

Sarmiento, J. L., Orr, J. C., and Siegenthaler, U.: A perturbation simulation of CO2 uptake in an ocean general circulation model, Journal of Geophysical Research: Oceans, 97, 3621–3645, https://doi.org/10.1029/91JC02849, _eprint: https://onlinelibrary.wiley.com/doi/pdf/10.1029/91JC02849, 1992.

Sarmiento, J. L., Monfray, P., Maier-Reimer, E., Aumont, O., Murnane, R. J., and Orr, J. C.: Sea-air CO2 fluxes and carbon transport: A comparison of three ocean general circulation models, Global Biogeochemical Cycles, 14, 1267–1281, https://doi.org/10.1029/1999GB900062, _eprint: https://onlinelibrary.wiley.com/doi/pdf/10.1029/1999GB900062, 2000.

https://doi.org/10.5194/egusphere-2025-523
Preprint. Discussion started: 13 February 2025
© Author(s) 2025. CC BY 4.0 License.

Stock, C. A., Dunne, J. P., Fan, S., Ginoux, P., John, J., Krasting, J. P., Laufkötter, C., Paulot, F., and Zadeh, N.: Ocean Biogeochemistry in GFDL's Earth System Model 4.1 and Its Response to Increasing Atmospheric CO $_2$, Journal of Advances in Modeling Earth Systems, 12, https://doi.org/10.1029/2019MS002043, 2020.

Takahashi, T., Sutherland, S. C., Wanninkhof, R., Sweeney, C., Feely, R. A., Chipman, D. W., Hales, B., Friederich, G., Chavez, F., Sabine, C., Watson, A., Bakker, D. C., Schuster, U., Metzl, N., Yoshikawa-Inoue, H., Ishii, M., Midorikawa, T., Nojiri, Y., Körtzinger, A., Steinhoff, T., Hoppema, M., Olafsson, J., Arnarson, T. S., Tilbrook, B., Johannessen, T., Olsen, A., Bellerby, R., Wong, C., Delille, B., Bates, N., and de Baar, H. J.: Climatological mean and decadal change in surface ocean pCO2, and net sea–air CO2 flux over the global oceans, Deep Sea Research Part II: Topical Studies in Oceanography, 56, 554–577, https://doi.org/10.1016/j.dsr2.2008.12.009, 2009.

Tans, P. P., Fung, I. Y., and Takahashi, T.: Observational Constraints on the Global Atmospheric CO2 Budget, 247, 1990.

Wanninkhof, R., Park, G. H., Takahashi, T., Sweeney, C., Feely, R., Nojiri, Y., Gruber, N., Doney, S. C., McKinley, G. A., Lenton, A., Le Quéré, C., Heinze, C., Schwinger, J., Graven, H., and Khatiwala, S.: Global ocean carbon uptake: magnitude, variability and trends, Biogeosciences, 10, 1983–2000, https://doi.org/10.5194/bg-10-1983-2013, 2013.